Review

Progress and Challenges of Vanadium Oxide Cathodes for Rechargeable Magnesium Batteries

Elena G. Tolstopyatova [1], Yulia D. Salnikova [1], Rudolf Holze [1,2,3,4,*] and Veniamin V. Kondratiev [1,*]

1   Institute of Chemistry, Saint Petersburg State University, 7/9 Universitetskaya Nab.,
    199034 Saint Petersburg, Russia
2   State Key Laboratory of Materials-Oriented Chemical Engineering, School of Energy Science and Engineering,
    Nanjing Tech University, Nanjing 211816, China
3   Chemnitz University of Technology, 09107 Chemnitz, Germany
4   Confucius Energy Storage Lab, School of Energy and Environment, Southeast University,
    Nanjing 210096, China
*   Correspondence: rudolf.holze@chemie.tu-chemnitz.de (R.H.); v.kondratev@spbu.ru (V.V.K.)

Abstract: Among the challenges related to rechargeable magnesium batteries (RMBs) still not resolved are positive electrode materials with sufficient charge storage and rate capability as well as stability and raw material resources. Out of the materials proposed and studied so far, vanadium oxides stand out for these requirements, but significant further improvements are expected and required. They will be based on new materials and an improved understanding of their mode of operation. This report provides a critical review focused on this material, which is embedded in a brief overview on the general subject. It starts with the main strategic ways to design layered vanadium oxides cathodes for RMBs. Taking these examples in more detail, the typical issues and challenges often missed in broader overviews and reviews are discussed. In particular, issues related to the electrochemistry of intercalation processes in layered vanadium oxides; advantageous strategies for the development of vanadium oxide composite cathodes; their mechanism in aqueous, "wet", and dry non-aqueous aprotic systems; and the possibility of co-intercalation processes involving protons and magnesium ions are considered. The perspectives for future development of vanadium oxide-based cathode materials are finally discussed and summarized.

Keywords: magnesium ion battery; cathode materials; electrochemical performance

1. Introduction

Magnesium ion batteries are among the promising power sources that can provide high energy density combined with increased environmental and operational safety at lower device costs mostly because of the high magnesium content in the Earth's crust [1–6]. The Mg/Mg^{2+} system provides metallic anodes offering a high theoretical specific capacity ($3834\ mAh \cdot cm^{-3}$), which is higher than that of metallic lithium ($2061\ mAh \cdot cm^{-3}$). It also provides an attractively low electrode potential ($-2.37\ V$) and forms metallic deposits without dendrites [1,4–6].

Due to these advantages, rechargeable magnesium ion batteries have attracted considerable and growing research interest in the field of post-lithium secondary batteries [7]. For comparison, Table 1 collects pertinent data on relevant negative electrode materials.

Systems with both non-aqueous and aqueous electrolytes are considered, in addition to the extended window of electrochemical stability available with water-in-salt electrolytes [8] has been discussed and extended into a quasi-solid state concept [9]. A first pouch cell demonstration has been reported [10].

Challenges for developing a practical magnesium full cell are related to all components, including in particular Mg^{2+}-containing electrolytes that would remain electrochemically stable with both a Mg anode and cathodes. Nonaqueous rechargeable magnesium batteries

also suffer from the complicated and moisture-sensitive electrolyte chemistry at magnesium electrode. Practical realization of a RMB is, in particular, handicapped by the absence of high-performance electrode materials due to the intrinsically slow Mg^{2+}-ion diffusion in solids.

Table 1. Selected data of relevant negative electrode materials for metal ion batteries [11].

Element	Atomic Mass	E_0, SHE/V	Gravimetric Capacity/mAh·g^{-1}	Volumetric Capacity/mAh·cm^{-3}
Li	6.94	−3.040	3860	2061
Na	23.0	−2.713	1165	1129
K	39.1	−2.924	685	610
Mg	24.31	−2.356	2206	3834
Ca	40.08	−2.840	1337	2072
Zn	65.41	−0.763	820	5855
Al	26.98	−1.676	2980	8046

Critical characteristics, such as specific capacity, rate capability, and cycling stability of RMBs, are strongly affected by the intrinsic electrochemical properties of the cathode, i.e., the positive electrode (following an earlier recommendation by Huggins [12,13]), and, in particular, the materials they are made of. There is continuous progress in the improvements of their properties.

Several earlier reviews [14–17] as well as selective overviews [10,18–23] on RMBs are available. They address cathode-related issues like electrode reaction kinetics particularly relevant for rate capability and mass utilization [24] and detrimental effects of particular properties attributed to Mg^{2+}-ions [25], highlight potential advantages of layered compounds [26], and provide mostly brief considerations and discussions of aspects concerning different intercalation-type cathode materials (like transition metal oxides, phosphates, chalcogenides, and Prussian blue analogues), but they are usually very short on considerations of their properties and mostly without an in-depth analysis of the reasons for the differences in functional properties (like specific capacity and power) and mechanism of intercalation processes regarding the latter class of materials. A focal issue is the high charge density of the magnesium ion with associated problems of strong interactions with a host material used in the positive electrode and associated slow diffusion. This also affects interfacial processes at the electrode/solution interface, and possibly even the electrolyte solution.

The number of investigations on different cathode materials for RMBs is rapidly increasing every year. Several reviews are published each year summarizing experimental progress on various cathode materials suitable for RMBs (transition metal oxides, sulfides, selenides, and other layered materials) [10,19,26–40]. However, given the large number of material classes and research areas, they are discussed too superficially, without more detailed consideration of the existing challenges.

Some more specialized reviews discuss and analyze reaction mechanisms in cathodes structure–kinetics correlations, strategies for improving the electrode kinetics [24], the role of the electrolyte composition in the intercalation processes of Mg^{2+}-ions [41], cathode materials and electrolytes for aqueous magnesium batteries [42], nanostructured cathode materials [43], and employing graphene and graphene-based materials to improve cathode materials [44].

Some reviews on RMBs have been dedicated to vanadium oxides solely. The structural characteristics and electrochemical performance of vanadium-based materials as RMB cathodes are discussed in [6,45,46]. The role of structural water molecules in vanadium oxide was analyzed in [47], the developments in application of vanadium oxide bronzes in metal ion batteries were discussed in [48], and the intercalation mechanisms in vanadium oxide were discussed in [49,50].

In this review, we will focus on the recent investigations of one of the promising and widely studied groups of cathode materials—layered vanadium oxides, including a systematic discussion of the achievements in their development and their possible improvement, the existing opinions on the mechanisms of charge–discharge processes in aqueous, "wet", and dry non-aqueous electrolytes, and strategies to optimize functional properties of these cathode materials. We believe that this specialized and detailed review will help researchers to optimize the functional properties of these cathode materials.

2. Vanadium Oxide-Based Cathodes

Why did we select vanadium oxides as cathode materials for RMBs for this review?

Although the radius of Mg^{2+}-ions (0.72 Å) is similar to that of Li^+-ions (0.76 Å), the intercalation of Mg^{2+}-ions into the same host materials is more difficult due to the difference in charge. The large charge/radius ratio of Mg^{2+}-ions results in their strong electrostatic interactions with cathode materials, making intercalation and diffusion processes sluggish. As a result, most cathode materials suitable for RMBs exhibit a low degree of magnesiation, large voltage hysteresis, and low rate capabilities. Therefore, it is important to develop high-performance cathode materials for RMBs.

Vanadium-based materials have high theoretical capacity and energy density resulting from the multiple valence states of vanadium. Many vanadium-based materials have a layered structure, and the interlayer can be enlarged and adjusted to favor the intercalation and diffusion of Mg^{2+}-ions into the cathode material.

Among vanadium-based materials, vanadium oxides are the most common and have numerous advantages for multivalent metal ion batteries. Vanadium oxides are cheap and abundant. Vanadium oxides with different structures have a variety of valence states ($V^{+3}/V^{+4}/V^{+5}$) and can be easily synthesized by a variety of methods. Vanadium oxide polymorphs with different lattice symmetries have different electronic properties and thus different metal ion insertion thermodynamics and kinetics. Different synthetic strategies offer possibilities to synthesize different polymorphic structures and to fit the obtained layered structures to different interlayer distances and to weaken (i.e., screen) the strong electrostatic interaction of Mg^{2+}-ions with the host lattice.

Among other cathode materials, the vanadium pentoxide family has been considered promising for RMBs due to the high theoretical capacity of V_2O_5 (294 mAh·g^{-1}, considering 1 mol of Mg^{2+} per mol of V_2O_5) and high working voltage of ≈2.4 V, resulting in a high specific energy (>600 Wh·kg^{-1}) [6,51–53]. Orthorhombic V_2O_5 was the first of the vanadium oxides to be investigated for Mg^{2+} intercalation.

In recent years, researchers have focused on other types of vanadium oxides like $V_2O_5 \cdot nH_2O$, $M_xV_2O_5 \cdot nH_2O$ (with M: intercalated foreign metal ion) [54], VO_2 [55,56], and others, and also specially designed mixed-valence composites, such as V_3O_7/VO_2 [57].

In the thermodynamically most stable α-phase, V_2O_5 has a layered structure consisting of alternating edge- and corner-sharing distorted VO_5 trigonal-bipyramidal coordination polyhedrons stacked along the *c*-axis with an interlayer spacing of 4.37 Å (Figure 1a). Vanadium oxide gels ($V_2O_5 \cdot nH_2O$) have bilayer crystal structures comprised of layered square-pyramidal VO_5 polyhedra in which V^{5+} is coordinated with five oxygen atoms. Water molecules are bound between the layers of V_2O_5 (Figure 1b). The reported water content *n* in $V_2O_5 \cdot nH_2O$ is usually about 1.6–2.0 moles per mole of V_2O_5 [58]. The layered structure provides channels for ion insertion and de-insertion (Figure 1b).

Brookite-phase vanadium dioxide VO_2(B) (Figure 1c) has a stable open framework. The crystal structure of VO_2(B) consists of corner- and edge-sharing VO_6 octahedra that provide three plausible migration channels along the *c*- and *b*-axes. It has a monoclinic symmetry with a space group of *C2/m*. Because the *b*-axis is the shortest unit cell dimension, crystals grow predominantly along the *b*-axis, forming one-dimensional morphologies such as nanowires, nanorods, and nanobelts. VO_2(B) is a promising candidate for RMBs due to its high theoretical capacity of 323 mAh·g^{-1} per one electron transfer for the V^{4+}/V^{3+} redox coupe [56].
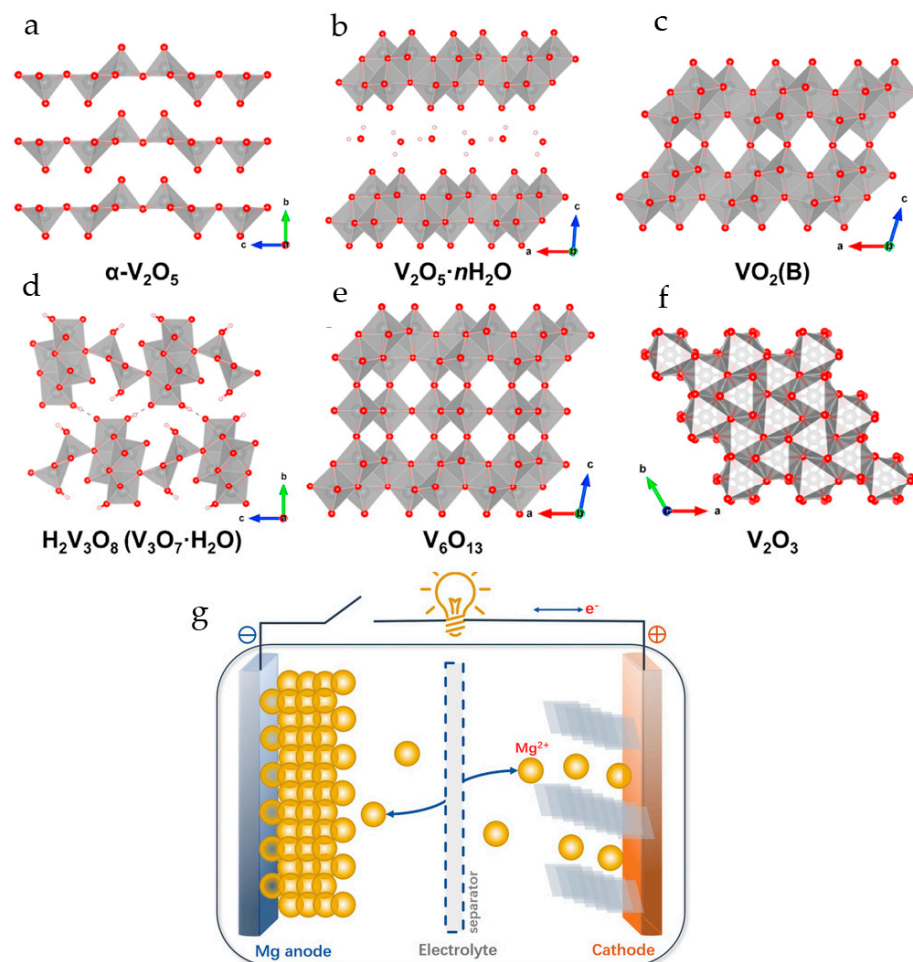
Figure 1. Crystal structures of vanadium oxides: (**a**) α-V$_2$O$_5$, (**b**) V$_2$O$_5 \cdot n$H$_2$O, (**c**) VO$_2$(B), (**d**) H$_2$V$_3$O$_8$ (V$_3$O$_7 \cdot$H$_2$O), (**e**) V$_6$O$_{13}$, (**f**) V$_2$O$_3$. (Reprinted with permission from [45]. Copyright 2023, Elsevier). (**g**) The working principle of the RMB. (Reprinted with permission from [21]. Copyright 2020, John Wiley and Sons).

Hydrated vanadium oxide (H$_2$V$_3$O$_8$, V$_3$O$_7 \cdot$H$_2$O, HVO) (Figure 1d) has an orthorhombic crystal structure and comprises V$_3$O$_8$ layers, consisting of edge- and corner-shared VO$_5$ square pyramids and VO$_6$ octahedra. In contrast to van der Waals forces in V$_2$O$_5$, vanadium oxide layers in HVO are linked by hydrogen bonds, which decrease the volume expansion/contraction during cycling.

The crystal structure of V$_6$O$_{13}$ (Figure 1e) is composed of corner- and edge-sharing distorted VO$_6$ octahedra, which form alternating single and double vanadium oxide layers connected by shared corners. V$_6$O$_{13}$ has high electrical conductivity at room temperature and has a high theoretical capacity of 417 mAh·g^{-1} when high-valent vanadium (V^{5+}/V^{4+}) is all reduced to V^{3+}.

The vanadium trioxide V$_2$O$_3$ (Figure 1f) possesses a tunnel-like 3D structure, which determines its good ion intercalation performance. The theoretical capacity of V$_2$O$_3$ is 357.5 mAh g^{-1} and 715.1 mAh g^{-1} for one- and two-electron redox processes.

Consideration of this class of insertion-type compounds allows to highlight the main strategic ways to design layered metal oxide cathodes and to consider, on these examples, the typical issues and mechanistic details often missing within broader overviews and reviews.

In particular, these issues should be focused on (i) the electrochemistry of intercalation processes in layered oxides (vanadium oxide V$_2$O$_5$ and its modifications), their mechanism in aqueous, wet, and dry non-aqueous aprotic systems (PC, AN), the possibility of co-

intercalation processes involving protons and magnesium ions; and (ii) the dependence of electrochemical properties on the modification of the interlayer space due to the inclusion of foreign metal ions, organic molecules (polymeric and others), and water molecules.

The basis for the selection of a suitable inorganic host material in metal ion battery technology is the reversible electrochemical intercalation processes associated with electrochemical redox processes with the recharging of metal ions and the accompanying reversible processes of insertion/removal of electrolyte cations into/from the host electrode material (Figure 1g). The driving force of these processes is the gradient of electrochemical potentials realized in the host materials. The three main factors affecting the intercalation and diffusion of metal ions are (i) steric factors, depending on the geometric size of intercalated metal ions and crystal structures providing the interstitial voids along ion hopping trajectories, (ii) desolvation of ions at injection, and (iii) electrostatic and other interactions of intercalated ions with the host materials.

Several innovative approaches have been proposed for layered oxide cathodes to successfully overcome all these challenges in the case of Mg^{2+}-intercalation. Among them is the strategy based on a significant increase in the interlayer spacing in layered materials by the synthesis of layered materials pre-intercalated/doped with foreign metal ions or organic molecules, which could facilitate Mg^{2+}-intercalation and diffusion in the host material. Another important feature of the increased interlayer spacing is the possible intercalation of solvated magnesium ions, avoiding the sluggish desolvation process at the interface.

Additional attention is given to the retention of water molecules in the host structures and the co-insertion of water molecules in the case of aqueous or wet non-aqueous electrolytes. The degree of reversible Mg^{2+}-insertion strongly depends on the "lubrication" of the layered channels. The selected strategic approaches are usually combined with more common measures, such as nanostructuring of materials, which results in shortening the solid state diffusion path for highly polarized Mg^{2+} in the host and increasing the surface area of the active grains. In the following, we discuss these issues in more detail, based on experimental examples from published original works.

2.1. Orthorhombic Vanadium Pentoxide V_2O_5

Orthorhombic vanadium pentoxide (α-V_2O_5) was the first compound in the family of vanadium oxides to be proposed for use as cathode in RMBs. Early works showed that its typical layered crystal structure with weak van der Waals forces is suitable for tuning the interlayer space, making it accessible for intercalation of Mg^{2+}-ions [29,59–61].

The electrochemical intercalation of Mg^{2+}-ions into orthorhombic V_2O_5 in a solid state RMB composed of a metallic Mg anode, a solid Mg-montmorillonite electrolyte, and a V_2O_5 cathode has been confirmed [59]. The quantitative estimation of magnesium intercalation was reported [60], where the authors reported that 0.66 mol of Mg can be intercalated into 1 mol of V_2O_5 by chemical intercalation in the dibutylmagnesium/heptane solution, which corresponds to a high specific capacity of 194 mAh·g^{-1}. This value is consistent with the capacity determined electrochemically in a 1 M $Mg(ClO_4)_2$/THF electrolyte.

A stronger indication that V_2O_5 is a potential cathode material for RMBs was the first publication on the ability of α-V_2O_5 to reversibly electrochemically intercalate Mg^{2+} in 1 M $Mg(ClO_4)_2$/AN electrolytes with water added to AN [61]. It was shown that the insertion of Mg^{2+} into V_2O_5 depends on the ratio between the amounts of H_2O and Mg^{2+} and on the absolute amount of H_2O in the electrolyte solution. The preferential solvation of Mg^{2+}-ions by water molecules facilitated the insertion process. The highest capacities of up to 170 Ah·kg^{-1} were obtained in acetonitrile solutions containing 1 M $Mg(ClO_4)_2$ + 1 M H_2O; however, the electrode had low cycling stability—only about 50 Ah·kg^{-1} was retained after 20 cycles.

To optimize the diffusion pathways of Mg^{2+} in V_2O_5 during the charge–discharge, orthorhombic V_2O_5 with particle size in the range of 20 to 50 nm obtained via a combustion

flame-chemical vapor condensation process was suggested [62]. The reversible capacity of the V_2O_5 in 0.5 M $Mg(ClO_4)_2$/PC was 180 mAh·g^{-1} at a current density 7.6 mA·g^{-1}.

During the discharge process, Mg^{2+}-ions are gradually inserted into the interlayer of V_2O_5 and become coordinated with the VO_5 pyramids, and the oxidation state of vanadium decreases from +5 to +4. The V^{4+}/V^{5+} redox pair endows V_2O_5 with a high potential of 2.66 V vs. Mg/Mg^{2+}. The overall reaction of the electrochemical insertion of Mg^{2+} ions into V_2O_5 as a RMB cathode material can be written as

$$V_2O_5 + x\ Mg^{2+} + 2x\ e^- \ \rightleftarrows \ Mg_xV_2O_5 \tag{1}$$

V_2O_5 has a high theoretical specific capacity of 294 mAh·g^{-1} when 1 mol of Mg^{2+} ion is inserted (x = 1) [28].

V_2O_5 forms metastable polymorphs (β-, γ-, δ-, ε-, and ζ-V_2O_5) in addition to the thermodynamically stable phase (α-V_2O_5). Some of them have been the subject of theoretical and experimental studies concerning RMBs.

First-principles calculations were performed to investigate Mg intercalation in the α- and δ-polymorphs of V_2O_5 [63]. It was supposed that the conversion of fully demagnesiated stable α-V_2O_5 into a two-phase structure consisting of fully magnesiated δ-V_2O_5 and fully demagnesiated α-V_2O_5 phases during the discharge process results in slow diffusion kinetics in V_2O_5 electrodes. It was shown that since the calculated α-phase migration barriers indicate poor Mg mobility, reversible Mg intercalation is only possible at very low rates and in small particles, and the δ-V_2O_5 polymorph exhibits superior Mg mobility, provided that the δ-V_2O_5 host structure can remain stable or metastable over a wide Mg concentration range. The first-principles calculations have also shown that the Mg^{2+}-ion diffusion barrier in δ-V_2O_5 (~0.6–0.8 eV) is lower than that in α-V_2O_5 (~0.975–1.1 eV) [64].

The DFT calculations have also shown that V_2O_5 undergoes a structural transformation from the α-phase to the ε-phase (ε-$Mg_{0.5}V_2O_5$) and δ-phase (δ-MgV_2O_5) as the concentration of intercalated Mg^{2+}-ions is increased [65].

The DTF calculations have shown a significant reduction in barriers for Mg diffusion in the β-V_2O_5 phase (0.65 eV) compared to α-V_2O_5 (>1 eV), leading to possibly fast charge–discharge rates of β-V_2O_5 as a cathode material for Mg^{2+}-ion batteries [66]. β-V_2O_5 synthesized at high pressure demonstrated large voltage hysteresis in a dry (<20 ppm of H_2O) 0.1 M $Mg(ClO_4)_2$/AN electrolyte and a maximum discharge capacity of 361 mAh·g^{-1} in GCD tests at C/25 [67].

The migration barriers for Mg^{2+} in ζ-V_2O_5 calculated by DFT were 0.62–0.86 eV [68], also suggesting its applicability in RMB cathodes. The metastable ζ-V_2O_5 obtained by topochemical extraction of the Ag^+ ion from ζ-$Ag_{0.33}V_2O_5$ also demonstrated large voltage hysteresis in $Mg(TFSI)_2$/AN electrolyte, and displayed a specific capacity of 90 mAh g^{-1} with insertion of up to 0.33 Mg^{2+} per formula unit [69]. Nanosized ζ-V_2O_5 had a discharge capacity of 130 mAh·g^{-1} and lower voltage hysteresis [70].

The experimental investigations also indicated possible multi-stage transformation during the Mg^{2+}-intercalation. Mg ion intercalation into nanoscale films of V_2O_5 deposited on Pt was studied [71]. It was shown that highly reversible Mg insertion/de-insertion is possible within V_2O_5 thin films. In the 0.5 M $Mg(ClO_4)_2$/AN electrolyte, the V_2O_5 thin film was cycled over a potential range of 2.2–3.0 V vs. Mg/Mg^{2+}, and had an initial capacity of 180 mAh·g^{-1} at a 0.15 mV s^{-1} scan rate, the capacity retention after 36 cycles was ~83%. The electrodes had 100% coulombic efficiency. The differential capacity plots (dQ/d$V - V$) obtained for low current density galvanostatic cycling revealed four different Mg^{2+}-insertion stages or processes with different thermodynamic and kinetic characteristics.

In order to check the inherent ability of α-V_2O_5 to intercalate Mg^{2+}, electrochemical tests were conducted in an ionic liquid electrolyte in [72]. The α-V_2O_5 cathode prepared from commercial vanadium oxide powder had a low reversible capacity of only 16 mAh·g^{-1} at 25 °C, which increased to 295 mAh·g^{-1} (at C/5) at 110 °C. This capacity corresponds

to reversible intercalation of 1 mol Mg^{2+} per unit formula. After 1 cycle at 110 °C, the electrochemical activity of α-V_2O_5 at room temperature was significantly enhanced (specific capacity of about 95 mAh·g^{-1} at C/5). The composition of the cathode after the thermal activation was $Mg_{0.2}V_2O_5$; accordingly, the activation resulted in an expanded interlayer spacing with Mg-pillaring, facilitating fast Mg^{2+}-migration. The reversible intercalation of Mg^{2+} into α-V_2O_5 was also observed during the characterization of the material composition, crystal structure, and redox state.

Thin films of orthorhombic V_2O_5 were grown on fluorine-doped tin oxide (FTO) glass electrodes using AACVD, and studied in aqueous solutions of $MgCl_2$ [73]. The material showed a specific discharge capacity as high as 427 mAh·g^{-1} at a high current density of 5.9 A·g^{-1} with 82% capacity retention after 2000 cycles. At a current density of 2.4 A·g^{-1}, the specific capacity was 170 mAh·g^{-1}, and when the current was returned to 5.9 A·g^{-1}, the cathode delivered 425 mAh·g^{-1}, corresponding to a capacity retention of 99%. The increase in the specific discharge capacity with increasing specific current was explained by the fast diffusion kinetics of Mg^{2+} in the metal oxide framework.

Several recent studies of V_2O_5 nanoclusters have shown that the use of vanadium-based nanoscale materials can improve the diffusion of Mg^{2+}-ions and provide high reversibility of intercalation processes. Highly dispersed vanadium oxide nanoclusters supported on porous carbon frameworks were synthesized using the ambient hydrolysis deposition method in order to improve the electrical conductivity of V_2O_5 [74]. The composite with 45 wt.% V_2O_5 had a surface area and pore volume of 593 m^2·g^{-1} and 2.8 cm^3·g^{-1}, respectively. Reversible intercalation of Mg^{2+} with an initial capacity of 350 mAh·g^{-1} (per V_2O_5) or 180 mAh·g^{-1} (per composite weight) at 40 mA·g^{-1} within the voltage range of 0.5–2.8 V was observed in 0.2 M $[Mg_2(\mu\text{-}Cl)_2(DME)_4][AlCl_4]_2$ in DME. During the subsequent five cycles, the capacity of the composite electrode decreased to 160 mAh·g^{-1} (per V_2O_5) or 90 mAh·g^{-1} (per composite).

*2.2. Nanostructured Vanadium Oxides*

The findings confirming slow diffusion kinetics in V_2O_5 and low capacities pointed at the necessity of modifying the structure of V_2O_5 for Mg battery electrode applications.

In most papers it was noted that strong electrostatic interactions between divalent Mg^{2+}-ions and lattice oxygen cause slow diffusion of Mg^{2+} in α-V_2O_5, and this is one of the main reasons for the unsatisfactory magnesium storage properties. Nanostructuring can increase the active surface area and reduce the diffusion distance to improve the electrochemical performance of α-V_2O_5. Various nanostructured vanadium oxide cathode materials with superior electrochemical performance were synthesized.

Hydrothermally synthesized V_2O_5 nanowires (Figure 2a) were used as a cathode in a magnesium ion system with 1 M $Mg(ClO_4)_2$/AN as an electrolyte and $Mg_xMo_6S_8$ ($x \approx 2$) as an anode [75]. V_2O_5 nanowires provided an initial discharge/charge capacity of 103/110 mAh·g^{-1} and a maximum discharge capacity of 130 mAh·g^{-1} in the sixth cycle at a C/20 rate in a full cell.

The synchrotron diffraction pattern of the pristine V_2O_5 nanowires (Figure 2b) showed a high degree of crystallinity in the material. All reflections were indexed in the orthorhombic α-V_2O_5 structure model with space group Pmn21 and lattice parameters a = 11.511 Å, b = 4.373 Å and c = 3.565 Å. The mechanism of Mg^{2+} insertion and extraction in V_2O_5 during the first two cycles was studied by *in operando* synchrotron diffraction (Figure 2c). It was shown that during the first discharge, the V_2O_5 phase accommodates Mg^{2+}-ions via a solid solution mechanism up to the stoichiometry of $Mg_{0.14}V_2O_5$, while the lattice parameters a and c increased and b decreased. During further magnesium uptake, a decrease in the amount of $Mg_{0.14}V_2O_5$ phase and an increase in the $Mg_{0.6}V_2O_5$ phase with constant cell parameters for both phases were observed; at the end of the first discharge, the phase ratio of $Mg_{0.14}V_2O_5$:$Mg_{0.6}V_2O_5$ was 13:87. In the second cycle, the material showed almost the same behavior during discharge, and at the end of the second charge V_2O_5 returned to its original structure.
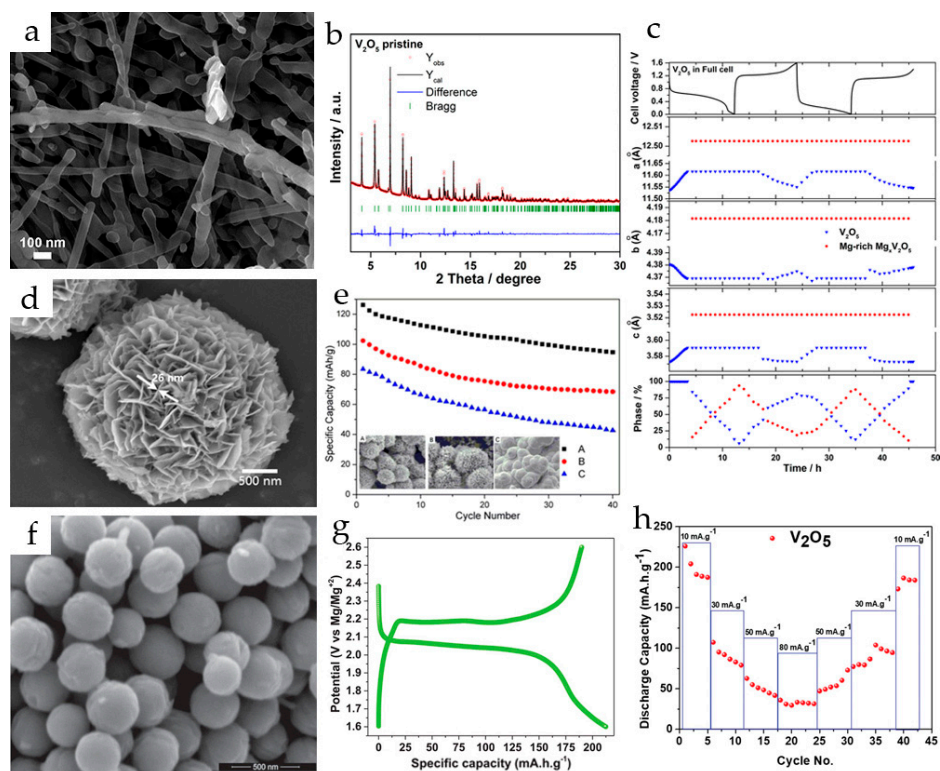
Figure 2. (**a**) SEM image of V_2O_5 nanowires, (**b**) synchrotron diffraction pattern of V_2O_5 nanowires, (**c**) structural parameters and phase ratios from diffraction patterns with Rietveld refinement during the first two charge–discharge cycles for V_2O_5. (Reprinted with permission from [75]. Copyright 2019, American Chemical Society.) (**d**) SEM image of V_2O_5 microspheres, (**e**) cyclic performance of V_2O_5 microspheres with the diameters of 3 (A), 7 (B), and 15 (C) μm. (Reprinted with permission from [76]. Copyright 2019, Springer). (**f**) SEM (scale 500 nm) image of V_2O_5 spheres, (**g**) first galvanostatic profile of V_2O_5 spheres at 10 mA·g^{-1}, (**h**) rate performance of V_2O_5 spheres. (Reprinted with permission from [77]. Copyright 2020, John Wiley and Sons).

Flower-like V_2O_5 microspheres composed of 25 nm thick nanosheets (Figure 2d) were synthesized via a surfactant-assisted hydrothermal procedure in [76]. The cathode produced from V_2O_5 microspheres with an average diameter of 3 μm delivered the initial discharge capacity of 126.2 mAh·g^{-1} at 50 mA·g^{-1} in 0.25 M Mg(AlCl$_2$EtBu)$_2$/THF, demonstrated good cycling stability (90.7 mAh g^{-1} after 80 cycles) and enhanced rate capability (60 mAh·g^{-1} at 200 mA·g^{-1}). The improved electrochemical performance of the V_2O_5 microflowers was explained by the increased specific surface area (13.7 m^2·g^{-1}) and flexibility. The microspheres with larger size (7 and 15 μm) or structural irregularities demonstrated lower capacities and cycling stability (Figure 2e). The charge–discharge mechanism was investigated by X-ray diffraction and X-ray photoelectron spectroscopy.

Monodisperse spherical V_2O_5 particles with a diameter of 230–250 nm were obtained in [77] (Figure 2f). The V_2O_5 spheres exhibited an initial discharge capacity of 225 mAh·g^{-1} (Figure 2g) and a stabile discharge capacity of 190 mAh·g^{-1} at 10 mA·g^{-1} in a dry Mg(ClO$_4$)$_2$/AN electrolyte. The rate performance of V_2O_5 spheres (Figure 2h) and long-term cycling stability at different current rates were good, and the specific discharge capacity of 55 mAh·g^{-1} was achieved at 50 mA·g^{-1} with 5% and 13% capacity fading after 50 and 100 cycles, respectively. The retention of 95% coulombic efficiency after 100 cycles and the stability of the phase and morphology confirmed the stability of the material during Mg^{2+}-ion intercalation/deintercalation.

$V_5O_{12}\cdot6H_2O$ nanoflowers formed by self-assembly of nanosheets were obtained by a one-step solvothermal method (Figure 3a) in [78]. The synthesized $V_5O_{12}\cdot6H_2O$ had uniform morphology with an average size of a nanoflower of 650 nm while the individual

nanosheets were about 25 nm thick (Figure 3b). For comparison, $V_5O_{12}\cdot 6H_2O$ nanoparticles were also synthesized. The galvanostatic tests revealed that both $V_5O_{12}\cdot 6H_2O$ nanoflowers and nanoparticles showed a similar activation process, the nanoparticles having a much lower capacity (Figure 3c). It was shown that the structural water in the interlayer of $V_5O_{12}\cdot 6H_2O$ improved the stability of the crystal structure and created more active sites for Mg^{2+} storage. The nanoflower morphology increased the active surface area, and enhanced the contact between the electrode material and the electrolyte, improving the diffusion kinetics of Mg^{2+}. The $V_5O_{12}\cdot 6H_2O$ nanoflowers had a high initial specific capacity of 234.3 mAh·g^{-1} and reversible capacity after activation of 153.2 mAh·g^{-1} at 10 mA·g^{-1} (in a 1:1 mixture of 0.8M PhMgCl and 0.4M AlCl$_3$ in anhydrous THF electrolyte) (Figure 3d), a good rate capability in the current range 50–500 mA·g^{-1} (Figure 3e), and long cycling stability (73.8% capacity retention after 1500 cycles at 100 mA·g^{-1}, i.e., 0.017% capacity loss per cycle). It was proposed that the layered structure of the $V_5O_{12}\cdot 6H_2O$ nanoflowers can accommodate the volume changes during the intercalation/deintercalation of Mg^{2+}, and the interlayer water molecules can serve as pillars enhancing the structural stability.

Ultrathin 2D V_6O_{13} nanosheets were synthesized via a microwave-assisted method [79]. Two pairs of redox peaks observed in CVs at 0.9/0.68 V and 1.15/1.33 V (vs. Mg/Mg^{2+}) correspond to the magnesiation/demagnesiation process, suggesting that it is a two-step process. The V_6O_{13} nanosheet cathode delivered a maximum discharge specific capacity of 324 mAh·g^{-1} at 20 mA·g^{-1} in 1 M Mg(ClO$_4$)$_2$/AN, corresponding to 3.22 mol of Mg^{2+} ions' insertion per unit formula of V_6O_{13}. At current densities of 40, 60, and 80 mA·g^{-1}, the reversible specific capacities were 278, 244, and 214 mAh·g^{-1}, respectively, indicating the good rate capability of the material. A high reversible capacity of 200 mAh·g^{-1} was retained after 30 cycles at 40 mA·g^{-1} with a ~100% coulombic efficiency.

Vanadium oxide nanotubes are advantageous for Mg^{2+}-intercalation due to their large interlayer distance, open ends, and large inner and outer diameters. The shape of the tubes is favorable for an ion insertion process because the diffusion path in the solid is shorter and the heterogeneous kinetics are faster at higher surface-to-bulk ratios. In addition, the tubes can provide electrolyte-filled channels or voids for fast Mg^{2+}-ion transportation to the insertion sites.

VO$_x$ nanotubes (with the nominal composition of VO$_{2.37}$[C$_{18}$H$_{40}$N]$_{0.26}$) were obtained from V_2O_5 and octadecylamine through a hydrothermal reaction [80]. The nanotubes had open ends and were 1–3 μm long, and their outer/inner diameter was 60–100 nm/15–40 nm, respectively. In an 0.25 M Mg(AlBu$_2$Cl$_2$)$_2$/THF electrolyte, the material exhibited good cycle performance, and the initial specific discharge capacity was 81 mAh·g^{-1} at 5 mA·g^{-1}. The Mg^{2+}-insertion into the VO$_x$ nanotubes was confirmed by the XPS and XPD results.

VO$_x$ nanotubes were obtained using a microwave-assisted hydrothermal method and low and high concentrations of the amine template, denoted as HT and LT, respectively [81]. The amount of the amine template did not affect the morphology of the VO$_x$ nanotubes; both types of nanotube had an average outer diameter of 80–100 nm and were 1–5 μm long. The performance of VO$_x$ nanotubes with various oxidation states (V^{3+}/V^{4+}/V^{5+}) as a cathode for RMB was studied in 0.5 M Mg(ClO$_4$)$_2$/AN solution. The kinetics of magnesium insertion and extraction depended highly on the oxidation state and bonding structure of the nanotubes' surface. The formation of V^{3+}-ions in highly reduced VO$_x$ nanotubes resulted in high initial discharge capacity (218 mAh·g^{-1} for HT-VO$_x$ and 230 mAh·g^{-1} for LT-VO$_x$ at 0.2 C (60 mA·g^{-1})), excellent cycling performance, and lower charge transfer resistance at the electrode/electrolyte interface compared to VO$_x$ nanotubes containing vanadium ions of higher oxidation states. Although the initial capacities of HT-VO$_x$ were lower than those of LT-VO$_x$, HT-VO$_x$ demonstrated better cycling performance, with capacity retention of 70.8% after 20 cycles. The coulombic efficiency of both materials increased while cycling.

The Mg^{2+}-ion insertion/extraction performance of VO$_x$-NTs was investigated in Mg(ClO$_4$)$_2$ tetramethylsilane-ethyl acetate (TMS-EA) electrolyte in comparison with an AN electrolyte [82]. The VO$_x$-NTs were prepared using a microwave-assisted hydrothermal

method starting with V_2O_5 and octadecylamine. As seen in the SEM and TEM images (Figure 3f,g), the VO_x-NTs were open-ended, multilayered tubular structures, with alternating arrangements of VO_x and amine layers. VO_x-NTs showed an initial capacity of more than 200 mAh·g^{-1} in de-aerated 0.5 M Mg(ClO$_4$)$_2$/AN electrolyte solution, but had poor capacity retention. Superior cycling performance and coulombic efficiency were observed for the VO_x-NTs in TMS and TMS-EA, although the initial discharge capacities in TMS-based electrolytes were lower (Figure 3h). It was shown that the TMS-EA solvent improved the cell performance due to the higher stability of TMS against oxidation and the strong Mg^{2+} coordination ability of EA. The initial discharge capacity of VO_x-NT in TMS-EA solution was 124 mAh·g^{-1} at 0.2 C (60 mA·g^{-1}), and the capacity retention was 70% after 80 cycles.
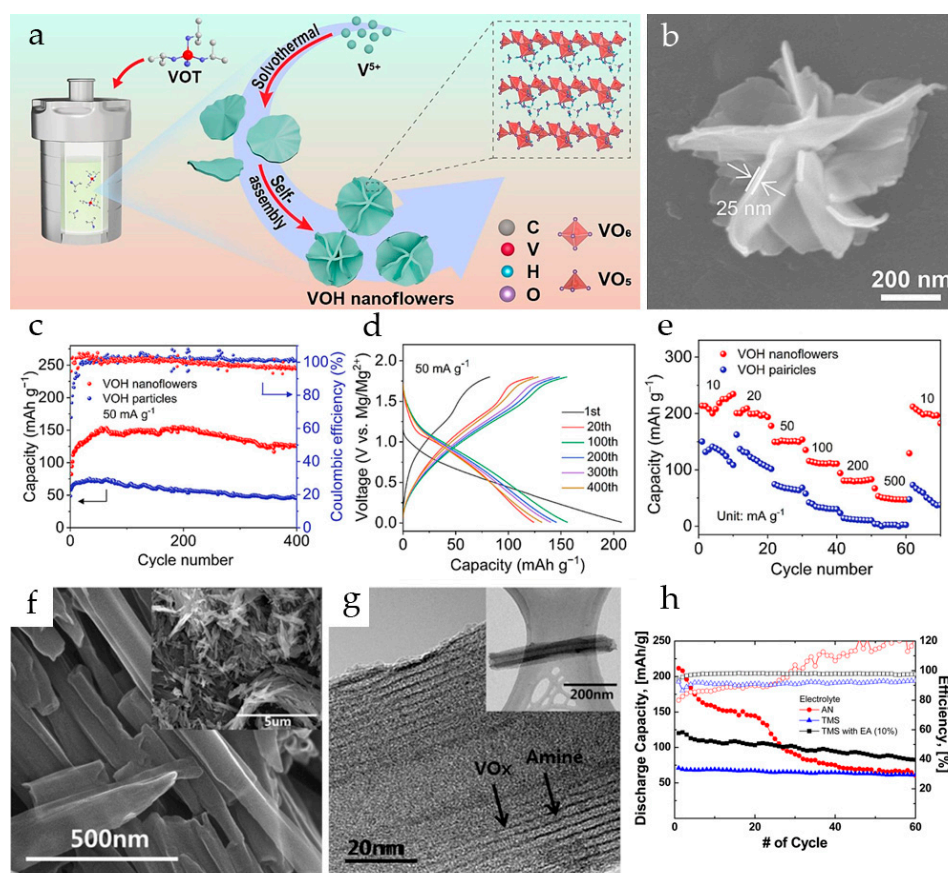
Figure 3. (**a**) Scheme of the preparation of $V_5O_{12}\cdot6H_2O$ nanoflowers, (**b**) SEM of a $V_5O_{12}\cdot6H_2O$ nanoflower, (**c**) cycling performance of $V_5O_{12}\cdot6H_2O$ nanoflowers and nanoparticles at 50 mA·g^{-1}, (**d**) discharge/charge profiles of $V_5O_{12}\cdot6H_2O$ nanoflowers, (**e**) rate capability of $V_5O_{12}\cdot6H_2O$ nanoflowers and nanoparticles. (Reprinted with permission from [78]. Copyright 2023, Elsevier). (**f,g**) High-resolution and (inset) low-resolution SEM and TEM images of VO_x-NTs, (**h**) discharge capacity and coulombic efficiency of VO_x-NT electrodes in AN, TMS, and TMS-EA electrolytes. (Reprinted with permission from [82]. Copyright 2016, American Chemical Society).

The electrochemical Mg^{2+}-ion intercalation and extraction in multi-walled vanadium oxide nanotubes VO_x-NTs was investigated in [83]. The VO_x-NTs had an open-ended structure of multilayer scrolls with an outer diameter of 50 nm and a length of a few μm, and the VO_x interlayer spacing was 2.7 nm. The initial specific discharge capacity for VO_x-NTs in 1 M Mg(ClO$_4$)$_2$/AN and in 1 M Mg(TFSI)$_2$/G2 was 146 ± 36 and 33 ± 12 mAh·g^{-1} at 5 mA·g^{-1}, respectively, since, as a rule, the cells with the Mg(TFSI)$_2$/G2 electrolyte provide lower initial capacities compared to Mg(ClO$_4$)$_2$/AN. In both electrolytes, the VO_x-NTs demonstrated poor capacity retention. The intercalation of Mg^{2+}-ions was confirmed by

ICP-AES. *In operando* scattering studies have shown that Mg^{2+}-ion intercalation into VOx-NTs is accompanied by an increase in the interlayer spacing and a loss of the long-range stacking order.

2.3. Bilayer V_2O_5

V_2O_5 gels can be synthesized by a sol–gel process from a variety of precursors. Xerogels and aerogels differ in the drying process that removes the solvent from the nanoscale pores and capillaries after the material is synthesized. Xerogels are dried at ambient conditions, resulting in a more compact and dense material than aerogels. Aerogels are dried by filling the pores and capillaries with a supercritical fluid and then cooling so that the pores are filled with a gas. This process allows the pores to remain intact and increases the surface area of the material. V_2O_5 aerogel has a surface area ~30 times larger than that of V_2O_5 xerogel [27].

V_2O_5 gels have an enhanced capacity for insertion/extraction of magnesium ions due to their water content. Furthermore, the increased surface area supports more efficient diffusion and provides more sites for insertion/extraction of magnesium ions, thus increasing the ability of the material to enable high-rate charge and discharge. In addition, the capacity increases due to the large surface area because there is less isolated bulk material that the intercalating ions cannot reach.

Amorphous V_2O_5 aerogels with high surface area, consisting of interpenetrating networks of water and V_2O_5 ribbons, are capable of accommodating 0.6–2 moles of Mg^{2+} per mole of V_2O_5 as a result of chemical insertion [84], or two moles formally corresponding to the reduction of V^{5+} to the V^{3+} state [85].

Bilayer $V_2O_5 \cdot nH_2O$ is generally considered to be amorphous due to the lack of long-range structural order, but at the nanoscale, a well-organized repetition of bilayers is observed. The synthesis route affects the morphology of $V_2O_5 \cdot nH_2O$. The reduced structural order, wide interlayer space, and short diffusion length in $V_2O_5 \cdot nH_2O$ allow reversible cation accommodation [86]. The interlayer structural water can increase the interlayer spacing, which is favorable for the intercalation of Mg^{2+}. The structural water molecules can partially shield the charge of Mg^{2+}, which leads to the improvement in the diffusion kinetics of Mg^{2+} in bilayer V_2O_5 [86].

The insertion of Mg^{2+} into V_2O_5 xerogel and V_2O_5 xerogel/C composite in aqueous $Mg(NO_3)_2$ electrolytes was studied [87]. The intercalation/deintercalation reaction of Mg^{2+}- ions was much faster in the case of the V_2O_5 xerogel/C composite as compared to the pure V_2O_5 xerogel. The addition of 10% carbon black during the synthesis of V_2O_5 xerogel/C composite allowed a significant improvement in the electrochemical behavior of this electrode material; the specific capacity of V_2O_5 xerogel/C composite in $Mg(NO_3)_2$ was $107\ mAh\cdot g^{-1}$, while pure V_2O_5 xerogel yielded $50\ mAh\cdot g^{-1}$.

V_2O_5 xerogel was prepared under microwave (MW) irradiation [88]. The structure and electrochemical properties of the V_2O_5 xerogel were compared with those of V_2O_5 prepared by conventional heat treatment. XRD revealed that the V_2O_5 xerogel prepared by MW irradiation was low-crystalline. The first discharge capacity of V_2O_5 prepared by MW irradiation was $175\ mAh\cdot g^{-1}$ at a 0.1 C rate in 0.3 M $Mg(ClO_4)_2$/PC solution, and the second discharge capacity increased to $463\ mAh\cdot g^{-1}$, indicating that Mg^{2+}-insertion increased after the first cycle. The capacity of V_2O_5 prepared by heat treatment at 200 °C was 138 and $190\ mAh\cdot g^{-1}$ for the first and the second cycles, respectively, and the capacity of V_2O_5 prepared by heat treatment at 300 °C was $77\ mAh\cdot g^{-1}$.

An amorphous V_2O_5 xerogel/graphite composite containing 10 wt.% synthetic graphite showed an initial deintercalation capacity of $77\ mAh\cdot g^{-1}$ at $10\ mV\cdot s^{-1}$ (~18 C rate) in $Mg(NO_3)_2$ aqueous electrolyte [89]. After ten cycles, the value decreased to $63.5\ mAh\cdot g^{-1}$. In GCD tests, a relatively high magnesium storage capacity of 62, 53, 47, and $44\ mAh\cdot g^{-1}$ was obtained at 2, 3, 4, and $5\ A\cdot g^{-1}$, respectively.

The scenario of Mg^{2+} and H_2O co-intercalation in nanocrystalline V_2O_5 xerogel was analyzed by first-principles calculations [90]. The models of fully relaxed structures of the

fully magnesiated and demagnesiated V_2O_5 xerogel, where two individual V_2O_5 layers are bound by long interlayer V–O bonds and the intercalated Mg atoms and H_2O molecules are located in the space between two bilayers, are shown in Figure 4a,b.
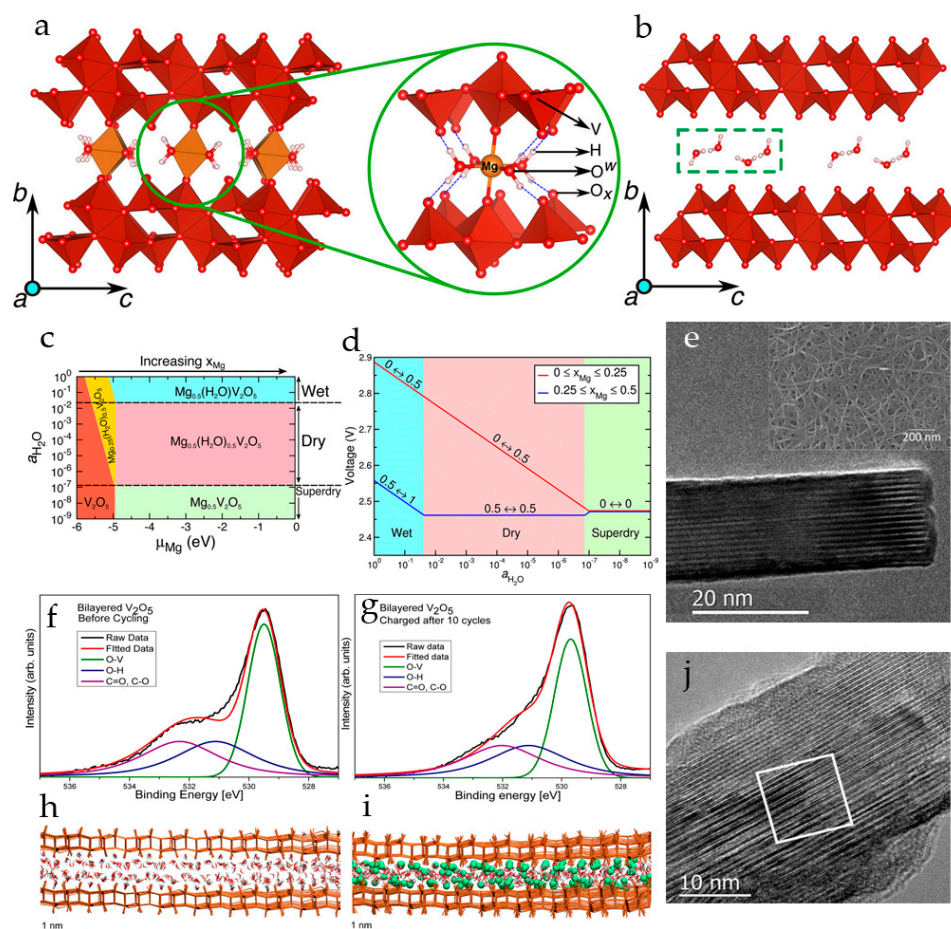
Figure 4. Structures of (**a**) fully magnesiated (xMg = 0.5) and (**b**) fully demagnesiated xerogel with one H_2O molecule per formula unit of V_2O_5, (**c**) potential phase diagram at 0 K of Mg-intercalated V_2O_5 xerogel as a function of water content in the electrolyte and Mg chemical potential (μMg = 0 corresponds to full magnesiation), (**d**) average Mg insertion voltage for low and high Mg concentrations as a function of water content in the electrolyte (aH$_2$O). (Reprinted with permission from [90]. Copyright 2016, American Chemical Society). (**e**) HRTEM of a nanoribbon of bilayered V_2O_5 (inset—SEM of the nanoribbon architecture on a carbon nanofoam substrate), (**f**,**g**) XPS spectra of bilayered V_2O_5 before and after 10 cycles of charging with Mg^{2+}-ions, and (**h**) MD simulation of the V_2O_5 bilayer immersed in water and (**i**) V_2O_5 bilayer (V in the +4 state) in the presence of Mg^{2+} ions in the presence of water, (**j**) HRTEM image of Mg-enriched V_2O_5. (Reprinted with permission from [91]. Copyright 2015, American Chemical Society).

Analysis of the stable phases of Mg-intercalated V_2O_5 xerogel at different voltages and in electrolytes with different water contents revealed a range of concentrations of intercalated Mg-ions in the V_2O_5 xerogel and H_2O in the electrolyte where there is no thermodynamic driving force for the water molecules to shuttle with Mg^{2+}-ions during electrochemical cycling (Figure 4c,d). It was also demonstrated that shuttling of water molecules with the Mg^{2+}-ions in wet electrolytes yields higher voltages than in dry electrolytes.

Highly hydrated nanoribbons of bilayer V_2O_5 with a large interlayer distance (13.5 Å) were electrodeposited on porous highly conductive carbon nanofoam [91]. This method also allowed effective incorporation of defects, water, and hydroxyl groups, which in turn

promoted electron transfer and (de)intercalation of highly charged Mg^{2+} ions. The "as-prepared" individual V_2O_5 nanoribbon is shown in an HRTEM image in Figure 4e. Mg^{2+} ions were incorporated into the as-prepared bilayer V_2O_5 cathodes by galvanostatic discharge at 20 μA to the potential 0.2 V (vs. Mg/Mg^{2+}). The specific capacity of 240 mAh·g^{-1} obtained after this preconditioning procedure suggests reduction of vanadium V^{5+} to V^{4+}. The electrode demonstrated reversible Mg^{2+} (de)intercalation in 1 M $Mg(ClO_4)_2/AN$ electrolyte with a capacity of 150 mAh·g^{-1} at C/15 rate. The O 1s XPS spectra before cycling and after 10 cycles of charging showed that strongly bound structural hydroxyl groups remain in the structure of bilayer V_2O_5 during cycling (Figure 4f,g), and act as a lubricant for reversible (de)intercalation of solvated Mg^{2+} ions between the layers of V_2O_5. Molecular dynamics simulations of a three-bilayer V_2O_5 model, shown in Figure 4h,i, suggested that upon insertion of Mg^{2+}-ions into the V_2O_5 structures, the spacing between bilayers decreases from ~12 to ~11 Å due to the interaction of Mg^{2+}-ions with bilayer apical oxygen and structural hydroxyl groups, but a significant amount of H_2O molecules remains in the structure, solvating the Mg^{2+} ions. The HRTEM image (Figure 4j) showed that after Mg^{2+}-ions were intercalated, the layered V_2O_5 structure featured a spacing of 6.0 to 6.4 Å, and the bilayer distance was not uniform across the whole imaged area.

The reversible insertion/extraction of Mg^{2+} into the $V_2O_5 \cdot nH_2O$ electrode accompanied by the co-intercalation of solvent molecules was demonstrated [92]. The $V_2O_5 \cdot nH_2O$ achieved a discharge capacity of 50 mAh·g^{-1} (0.25 Mg per $V_2O_5 \cdot nH_2O$) in a $Mg(TFSI)_2/G2$ (diglyme) electrolyte at a current density of 20 mA·cm^{-2}. It was shown that the process of Mg^{2+} intercalation into $V_2O_5 \cdot nH_2O$ involves the formation of new phases, while the bilayer spacing expands/contracts. The large interlayer spacing of bilayer V_2O_5 allowed the reversible co-intercalation of Mg^{2+} and solvent molecules.

Bilayered nanostructured $V_2O_5 \cdot nH_2O$ 2D nanopapers with oxygen defects (BL-HVOd NPS) with improved Mg^{2+} insertion/extraction kinetics were obtained [93]. The interlayer water molecules effectively stabilized the expanded interlayer spacing (10.6 Å) in BL-HVOd NPS and shielded the electrostatic interaction between Mg^{2+}-ions and BL-HVOd NPS lattice, improving diffusion kinetics during repeated cycling (the $\log(D_{Mg}^{2+})$ value was in the range from -8.3 to -9.5 during charge and discharge). The nanopaper structure of BL-HVOd NPS enhanced electrolyte/electrode contact and reduced the diffusion path of Mg^{2+}-ions, improving the rate performance. Cells with a BL-HVOd NPS cathode, AC anode, and 2 M $Mg(CF_3SO_3)_2$ aqueous electrolyte demonstrated a reversible capacity of 162.8 mAh·g^{-1} at 0.2 A·g^{-1} and high cyclic stability with 88% capacity retention after 2000 cycles at 10 A·g^{-1}. This was attributed to the contribution of oxygen defects.

Bilayer V_2O_5 is a promising cathode material for RMBs, but the low electronic conductivity of bilayer V_2O_5 is still a challenge that hinders its further application in RMBs. The main strategy to solve this problem is the modification of V_2O_5 with highly conductive materials or the pre-intercalation of metal ions to improve the conductivity of bilayer V_2O_5 and promote the ionic and electronic transport.

2.4. Nanocomposites of V_2O_5 with Conductive Carbons

The use of conductive carbons as additives for the improvement in electrical conductivity of V_2O_5 has also been studied in a large number of works.

Mg^{2+} ion intercalation into a V_2O_5/carbon composite, consisting of aggregated carbon particles (30–100 nm) covered with a thin layer (<100 nm) of V_2O_5 xerogel, in 1 M $Mg(ClO_4)_2/AN$ electrolyte, was reported in [94,95]. Mg^{2+} insertion into V_2O_5 xerogel/C composites and accompanying structural changes were studied [94]. In the cyclic voltammogram for the V_2O_5 xerogel/C composite in 1 M $Mg(ClO_4)_2/AN$, two broad cathodic peaks associated with the Mg^{2+}-insertion process were observed, pointing at the existence of two different Mg intercalation sites in the V_2O_5 xerogel. *Ex situ* FT-IR spectra suggested that Mg^{2+} is inserted into inner layer sites of V_2O_5 at -0.15 V and into the interlayer sites at -0.65 V vs. Ag/Ag^+. The reversibility of Mg^{2+} intercalation/deintercalation was confirmed by FT-IR and XRD. The V_2O_5/carbon composite showed higher capacity than a

conventional V_2O_5 electrode. It was assumed that the Mg^{2+} diffusion into the interlayer is slow, but since the V_2O_5/C composite has a large interlayer distance and short diffusion length compared to the normal xerogel of V_2O_5, the interlayer site could be utilized more effectively for Mg^{2+}-insertion.

With a V_2O_5 gel/carbon composite, insertion of 1.84 mol Mg per 1 mol V_2O_5 in the first cycle at a scan rate of 0.1 $mV \cdot s^{-1}$ was found, resulting in a specific capacity of 540 $mAh \cdot g^{-1}$ (per V_2O_5 mass) [95]. In GCD tests, at a current density of 1.0 $A \cdot g^{-1}$ the composite electrode showed a capacity of about 600 $mAh \cdot g^{-1}$, and at a high current density of 20 $A \cdot g^{-1}$ the capacity of about 300 $mAh \cdot g^{-1}$ was maintained. The capacity of the carbon-free V_2O_5 xerogel electrode at 1.0 $A \cdot g^{-1}$ was only 150 $mAh \cdot g^{-1}$, and at 20 $A \cdot g^{-1}$ it was less than 10% of the capacity of the composite electrode. Thus, homogeneous mixing of a V_2O_5 sol with carbon particles, resulting in the formation of a thin layer of V_2O_5 gel around the carbon particles, was effective in improving the Mg^{2+} intercalation behavior. The reduction in the Mg^{2+} diffusion length in V_2O_5 and the improvement in the electronic conductivity by the carbon particles resulted in high capacities, especially at high current densities. The composites of vanadium oxide with graphene are expected to advance the RMB performance by providing rapid electron transport and easy Mg^{2+}-diffusion due to the large surface area and excellent structural stability.

The synthesis of V_2O_5/graphene (GNP) nanoparticles by a ball milling technique was attempted in [96] to enhance the electrochemical performance of V_2O_5. The full cell with a Mg anode, $(V_2O_5)_{1-x}/GNP_x$ cathode, and $MgNO_3 \cdot 6H_2O$/tetraethylene glycol dimethyl ether electrolyte yielded an initial capacity of ~90 $mAh \cdot g^{-1}$ at a low current density, while Mg/V_2O_5 cells exhibited the initial discharge capacity of ~100 $mAh \cdot g^{-1}$ under the same testing conditions. The capacities dropped to half the initial value on the second cycle and then the cells short-circuited, probably due to the incompatible electrolyte.

A composite of V_2O_5 with graphene oxide (GO/V_2O_5) was prepared by a solvothermal method [97]. SEM revealed that the V_2O_5 microparticles were wrapped around GO sheets, and TEM micrographs demonstrated the tight contact between GO and V_2O_5 microparticles. The good contact and dispersion of the composite components provided improved electrochemical performance of the material. The GO/V_2O_5 cathode was tested in coin cells with a Mg foil anode and 0.25 M $Mg(AlCl_2EtBu)_2$/THF as an electrolyte. The GCD measurements showed an initial discharge capacity of GO/V_2O_5 of 178 $mAh \cdot g^{-1}$ at 0.2 C, which faded to 160 and 150 $mAh \cdot g^{-1}$ in the second and third cycle, respectively, due to formation of a Mg passivation layer, but still remained at 140 $mAh \cdot g^{-1}$ after 20 cycles.

rGO-decorated hydrated V_2O_5 nanowire composites with different contents of crystal water have been synthesized by a sol–gel method with subsequent freeze-drying [98]. The $V_2O_5 \cdot nH_2O$/rGO aerogel with a water content of 12.3% and large lattice spacing of 1.13 nm had a highly porous, interconnected 3D structure with V_2O_5 nanowires anchored on rGO (Figure 5a). The $V_2O_5 \cdot n H_2O$/rGO electrode showed a capacity of 280 $mAh \cdot g^{-1}$ at 100 $mA \cdot g^{-1}$ in a 0.5 M $Mg(TFSI)_2$/AN electrolyte, a capacity retention of 81% after 200 cycles, and a coulombic efficiency of 99%. At 50 $mA \cdot g^{-1}$ the capacity was 320 $mAh \cdot g^{-1}$. The nanocomposite displayed a wide working temperature range (~ 30–55 °C). As shown in Figure 5b, at 55 °C a high discharge capacity of ~200 $mAh \cdot g^{-1}$ was achieved, much higher than the capacity of 120 $mAh \cdot g^{-1}$ at room temperature. A reversible capacity of 40 $mAh \cdot g^{-1}$ was delivered at −30 °C. The improved electrochemical performance of the material was attributed to the shielding effect of crystal water as well as the synergistic effects of rGO, which provided Mg diffusion pathways, high surface area, and structural stability.

A three-dimensional structure of V_2O_3 nanoparticles with reduced graphene oxide (rGO) with improved conductivity and structural stability was prepared by spray-drying of a dispersed solution [99]. In the 0.3 M $Mg(TFSI)_2$/AN electrolyte solution, V_2O_3@rGO microspheres demonstrated a high specific capacity (291.3 $mAh \cdot g^{-1}$ at 50 $mA \cdot g^{-1}$) and improved rate performance (185.3 $mAh \cdot g^{-1}$ at a high current density of 2 $A \cdot g^{-1}$) compared to pure V_2O_3 (~80 $mAh \cdot g^{-1}$). Excellent cycling stability (88.5% capacity retention after

1000 cycles at 0.5 A·g^{-1}) with coulombic efficiency close to 100% was achieved. V$_2$O$_3$@rGO delivered a capacity of 472.1 mAh·g^{-1} in the GITT study, and the calculated diffusion coefficient of Mg^{2+} in the V$_2$O$_3$@rGO structure was 3.4×10^{-11} cm^2·s^{-1}.

A hierarchical V$_2$O$_3$@C structure with an accordion-like vanadium oxide/carbon heterointerface was synthesized from vanadium-based metal organic frameworks (Figure 5c) [100]. The mesoporous V$_2$O$_3$@C nanorods had a length of 250–300 nm, elongated pores of 30–50 nm (Figure 5d), and a BET surface area of 114.6 m^2·g^{-1}. The V$_2$O$_3$@C demonstrated a capacity of 354.8 mAh·g^{-1} at a current density of 500 mA·g^{-1} and an ultra-high capacity of 130.4 mAh·g^{-1} at 50 A·g^{-1} in 0.3 M Mg(TFSI)$_2$/AN(H$_2$O) with a coulombic efficiency of 99.6% and a capacity retention of 60.0% (1000 cycles, 500 mA·g^{-1}). To verify the advantages of hierarchical accordion-like heterointerfaces, the rate performance of the V$_2$O$_3$@C electrodes was compared with that of bulk-V$_2$O$_3$/AC and bulk-V$_2$O$_5$/AC electrodes prepared with activated carbon in the same ratio as in V$_2$O$_3$@C. As shown in Figure 5e, the specific capacity of bulk-V$_2$O$_3$/AC at 200 mA·g^{-1} (203.2 mAh·g^{-1}) is four times higher than of bulk-V$_2$O$_5$/AC (54.9 mAh·g^{-1}) due to the anodic hydration of the V$_2$O$_3$ phase, occurring in bulk-V$_2$O$_3$/AC upon the first charging. The crystalline structure of V$_2$O$_3$ was reconstructed into a V$_3$O$_7$·H$_2$O@C through an anodic hydration reaction upon the first cycle. The cell was disassembled under an inert atmosphere and the V$_3$O$_7$·H$_2$O@C electrode was retested in a 0.3 M Mg(TFSI)$_2$/AN electrolyte, where the specific capacity of the V$_3$O$_7$·H$_2$O@C electrode was 259.3 mAh·g^{-1} at 500 mA·g^{-1}. The capacity difference of 33.9 mAh·g^{-1} between the two electrolytes indicated that the capacity contributed by protons in the water-containing electrolyte is about 13% of the total capacity. The higher overpotential of the V$_3$O$_7$·H$_2$O@C electrode in water-free electrolyte solution resulted from the slower diffusion of Mg^{2+}-ions. In a full cell with a Mg anode and a 0.3 M Mg(TFSI)$_2$ + 0.25 M MgCl$_2$/DME electrolyte within the voltage range of 2.25 V vs. Mg/Mg^{2+}, the V$_2$O$_3$@C exhibited a capacity of 245.1 mAh·g^{-1}.

2.5. Foreign Cation Pre-Intercalated Vanadium Oxides

The rich valence state variation of vanadium and the easy distortion of V–O polyhedra lead to the ability of V–O structure adaptation to incorporate different cations. The resulting derivatives with an A–V–O structures (A—metal ion or NH$_4^+$) are called vanadates or foreign cation pre-intercalated vanadium oxides.

The pre-intercalation strategy has been widely recognized as a way to improve the properties of vanadium oxide cathodes for RMBs by increasing the interlayer space due to the pillaring effect combined often with improved stability of the obtained structures, allowing reversible insertion/extraction of Mg^{2+}-ions. The analysis of the results of different works shows that, in most cases of pre-intercalated ions, a dual effect of structure expansion and void hydration takes place.

It should be noted that the pre-intercalation of cations, with its positive effects on increasing the interlayer spacing of V$_2$O$_5$ bilayers, also has some drawbacks. The most important one is that the introduction of electrochemically inactive cations leads to a decrease in specific capacitance. Therefore, the necessary optimization of cathode materials requires a balance between structural and stability factors on the one hand, and the improvement of specific capacities on the other hand.

The differences in the active material composition (especially water content), electrode processing and morphology, and electrolyte system make it difficult to compare results from different groups.

Among the cations used for pre-intercalation of vanadium oxides for RMBs are mono-, bi-, and tri-valent ions: Na$^+$ [101–104], NH$_4^+$ [105,106], Mg^{2+} [107–110], Mn^{2+} [111], Ca^{2+} [112], and Al^{3+} [113].

NaV$_3$O$_8$·1.69H$_2$O nanobelts were synthesized from commercial V$_2$O$_5$ powder by a solvothermal procedure under ambient conditions (Figure 6a) [102]. The cells with a Mg anode and all-phenyl complex electrolyte demonstrated an initial discharge capacity of 150 mAh·g^{-1} and 110 mAh·g^{-1} after five cycles at a current density of 10 mA·g^{-1}. The

GCD curves of $NaV_3O_8 \cdot 1.69H_2O$ at different current densities (Figure 6b) showed several plateaus during the charging and discharge process, due to the multistep redox reactions responsible for the insertion/extraction of Mg^{2+} ions. The limited specific capacity of the cells was attributed to the trapping of Mg^{2+} ions in the lattice of NaV_3O_8. The cathodes demonstrated high cyclic stability with 80% capacity retention after 100 cycles at 50 mA·g^{-1}.
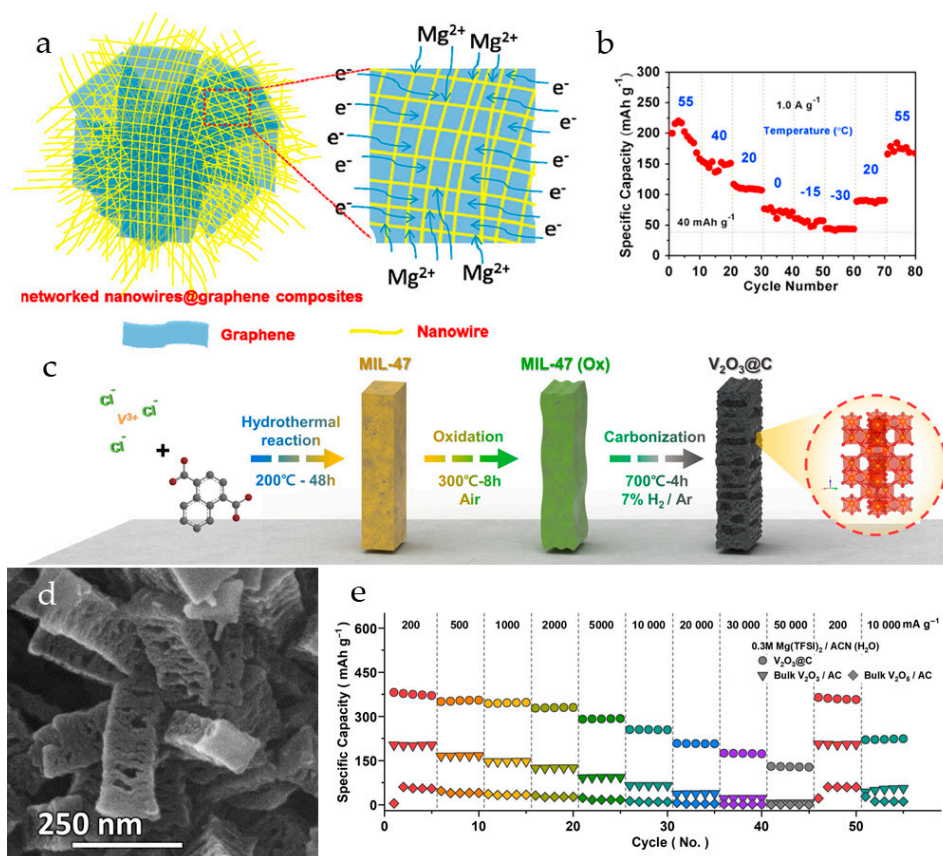

Figure 5. (**a**) Scheme of $V_2O_5 \cdot nH_2O$@rGO nanocomposite with electron/ion transport pathways, (**b**) cycling performance of $V_2O_5 \cdot nH_2O$@rGO at 1.0 A·g^{-1}, (**c**) discharge capacity $V_2O_5 \cdot nH_2O$@rGO at various temperatures at 1.0 A·g^{-1}. (Reprinted with permission from [98]. Copyright 2015, Elsevier). (**c**) Scheme of the synthesis of V_2O_3@C from MOFs, (**d**) SEM image of V_2O_3@C, (**e**) rate capabilities of V_2O_3@C, bulk-V_2O_3/AC and bulk-V_2O_5/AC. (Reprinted with permission from [100]. Copyright 2024, John Wiley and Sons).

Pre-intercalating of alkali ions (Li$^+$, Na$^+$, K$^+$) into layered vanadium oxide was studied in [101]. It was shown that the interlayer spacing of Li-, Na-, K-intercalated V_3O_8 increased regularly with the size of the pre-intercalated cations. The cycling performance of cathodes for Mg^{2+} storage was enhanced with the bigger radius of pre-intercalated ion (Figure 6c); after 30 cycles the capacity retention of KV_3O_8 was 88.6%, compared to 85.78% of NaV_3O_8 and 42.2% of LiV_3O_8, although the specific capacity of KV_3O_8 was the lowest (37.56 mAh·g^{-1}). The initial specific capacity of LiV_3O_8 and NaV_3O_8 at 100 mA·g^{-1} was 252.2 and 204.16 mAh·g^{-1}, respectively (Figure 6d). Based on structural analysis and electrochemical tests, it was concluded that pre-intercalation with Na$^+$ resulted in a more stable interlayer structure, allowing free Mg^{2+} diffusion and preventing destructive collapse of the layers during the charge–discharge.

The interlayer spacing of V_2O_5 was expanded in [103] by introducing Na$^+$-ions in the crystal lattice. NaV_6O_{15} (NVO) free of crystal water was synthesized and studied as a cathode material for RMBs with anhydrous 0.5 M $Mg(ClO_4)_2$/AN electrolyte solution. It was shown that the introduction of Na$^+$-ions enhanced the diffusion kinetics of Mg^{2+} ions ($D_{Mg^{2+}}$ during the discharge process was in the range of 7.55×10^{-13} to

2.41×10^{-11} cm$^2 \cdot$s^{-1} according to GITT), and improved the stability of the layered structure. NVO exhibited high initial discharge capacity of 213.4 mAh$\cdot$g^{-1} at the current density of 10 mA$\cdot$g^{-1}, good capacity retention (87% after 100 cycles at 20 mA$\cdot$g^{-1}), and good rate capability. The *ex situ* XRD showed that the mechanism of Mg^{2+} storage in NVO is reversible intercalation/de-intercalation. The DFT calculation results indicated that during the intercalation process, Mg^{2+}-ions tend to occupy the semi-occupied sites of Na$^+$ in the NVO.
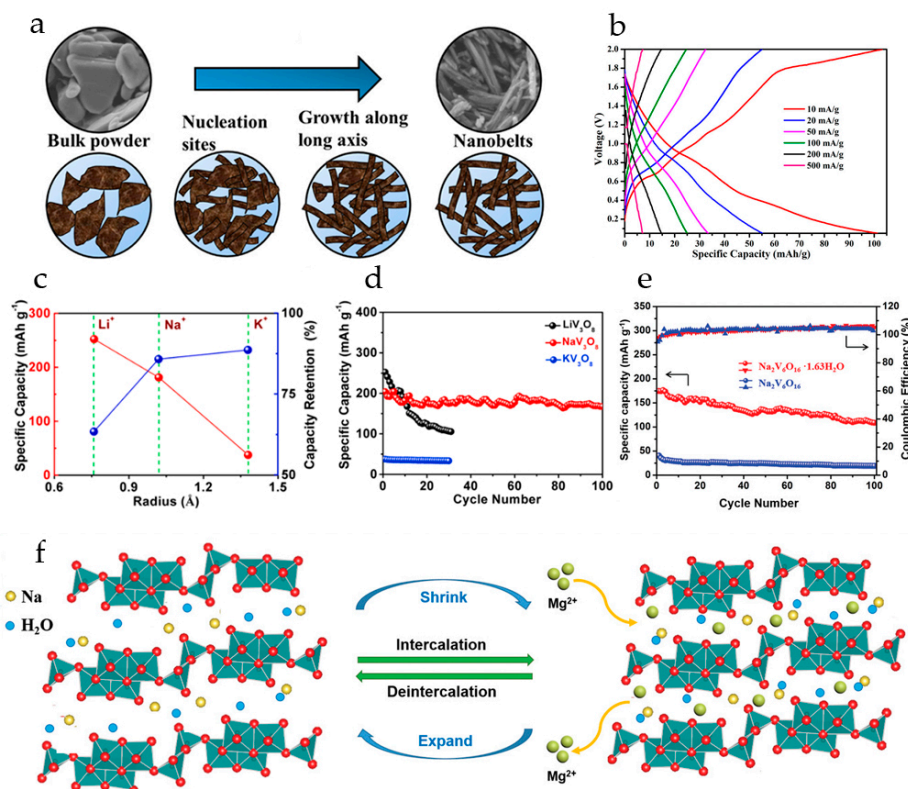
Figure 6. (**a**) Scheme of the growth mechanism of the NaV$_3$O$_8 \cdot$1.69H$_2$O nanobelts from V$_2$O$_5$, (**b**) charge–discharge curves of NaV$_3$O$_8 \cdot$1.69H$_2$O at current densities 10–500 mA$\cdot$g^{-1}. (Reprinted with permission from [102]. Copyright 2018 American Chemical Society). (**c**) Specific capacity of alkali ion (Li$^+$, Na$^+$, K$^+$) pre-intercalated V$_3$O$_8$ at 100 mA$\cdot$g^{-1} and the capacity retention after 30 cycles, (**d**) cycling performance of alkali ion pre-intercalated V$_3$O$_8$ at 100 mA$\cdot$g^{-1}. (Reprinted with permission from [101]. Copyright 2019, Elsevier). (**e**) Cyclic performance of Na$_2$V$_6$O$_{16}$ and Na$_2$V$_6$O$_{16} \cdot$1.63H$_2$O at 50 mA$\cdot$g^{-1}, (**f**) scheme of Mg^{2+} intercalation/deintercalation into Na$_2$V$_6$O$_{16} \cdot$1.63H$_2$O during the charge–discharge processes. (Reprinted with permission from [104]. Copyright 2020, John Wiley and Sons).

Water-pillared Na$_2$V$_6$O$_{16} \cdot$1.63H$_2$O nanowires obtained in [104] displayed high performance in magnesium storage. In a cell with a Mg(TFSI)$_2$/DME electrolyte and an AC anode, Na$_2$V$_6$O$_{16} \cdot$1.63H$_2$O exhibited a high specific capacity of 175 mAh$\cdot$g^{-1} at 0.05 A$\cdot$g^{-1}, long-term cycling performance, and $\approx$100% coulombic efficiency. Under the same testing conditions, annealed Na$_2$V$_6$O$_{16}$ delivered a low specific capacity of only 40 mAh$\cdot$g^{-1} (Figure 6e). Na$_2$V$_6$O$_{16} \cdot$1.63H$_2$O cathodes demonstrated a discharge voltage plateau at around 2.0 V (vs. Mg/Mg^{2+}), ascribed to the Mg^{2+} ion intercalation into the bilayer structure. According to *ex situ* XRD analysis, Na$_2$V$_6$O$_{16} \cdot$1.63H$_2$O possesses a very stable structure for reversible Mg^{2+} ion intercalation/deintercalation. During the discharge, Mg^{2+}-intercalation is accompanied by shrinkage of the interlayer space (Figure 6f). During subsequent charge–discharge processes, the Mg^{2+}-ions can reversibly intercalate/deintercalate into the Na$_2$V$_6$O$_{16} \cdot$1.63H$_2$O layers. The water molecules acting as "pillars" stabilize the layered structure and effectively shield the high charge density of Mg^{2+}-ions.

Magnesiated V_2O_5 xerogel with the formula $Mg_{0.1}V_2O_5 \cdot 1.8H_2O$ was synthesized in [109] by a low-temperature procedure. The material had an initial discharge capacity of 300 mAh·g^{-1} in 0.5 M $Mg(TFSI)_2$/AN. A capacity of ~250 mAh·g^{-1} was maintained over eight cycles at a C/10 rate, consistent with an insertion of 1 equivalent of Mg^{2+} per formula unit. No change in the interlayer distance (12.3 Å) was observed upon cycling of $Mg_{0.1}V_2O_5 \cdot 1.8H_2O$ electrodes.

Mg-inserted $V_2O_5 \cdot$xerogel was prepared via an ion removal sol–gel method in [114]. The $Mg_{0.1}V_2O_5 \cdot 2.35H_2O$ cathode displayed a high electrode potential of 3.0 V (vs. Mg/Mg^{2+}), high energy density of 420 mWh·g^{-1}, and a discharge capacity of 140 mAh·g^{-1} at a 0.1 C rate.

Mg^{2+} pre-intercalated hydrated vanadium oxide nanowires with bilayer structure, $Mg_{0.3}V_2O_5 \cdot 1.1H_2O$, were synthesized in [110] from α-V_2O_5 using a hydrothermal approach. The reaction of α-V_2O_5 with H_2O_2 lowers the valence state of V, resulting in structural transformation of VO_5 square pyramids to VO_6 octahedra, and a large number of H_2O molecules are embedded into the interlayer. This results in a bilayer structure with a larger interlayer space, providing ample channels for the subsequent insertion of Mg^{2+} ions. As a result of the coordination between Mg^{2+} and lattice oxygen, the insertion of Mg^{2+} ions into the layers leads to layer slippage and shrinkage (Figure 7a). In order to investigate the role of Mg^{2+} ions and lattice water molecules, $V_2O_5 \cdot nH_2O$ and $Mg_{0.3}V_2O_5$ nanowires were also prepared. In $Mg_{0.3}V_2O_5 \cdot 1.1H_2O$, the intercalated Mg^{2+} ions work together with crystal water to provide wide channels for electrolyte ion transport during the charge–discharge process. $Mg_{0.3}V_2O_5 \cdot 1.1H_2O$ possessed high electronic conductivity, fast Mg^{2+} reaction kinetics, and good structural stability. The charge and discharge curves of $Mg_{0.3}V_2O_5 \cdot 1.1H_2O$, $V_2O_5 \cdot nH_2O$ and $Mg_{0.3}V_2O_5$ at 0.1 A·g^{-1} in a cell with 0.3 M $Mg(TFSI)_2$/AN electrolyte and an activated carbon anode are shown in Figure 7b. $Mg_{0.3}V_2O_5 \cdot 1.1H_2O$ exhibited three discharge voltage plateaus at 3.02, 2.25, and 1.40 V (vs. Mg/Mg^{2+}), which can be attributed to the multi-step Mg^{2+} intercalation in the bilayer structure. $Mg_{0.3}V_2O_5 \cdot 1.1H_2O$ delivered high capacity (164 mAh·g^{-1} at 0.1 A·g^{-1}), corresponding to the insertion of 0.5 Mg^{2+} ions per formula unit. $V_2O_5 \cdot nH_2O$ had a similar charge–discharge curve, with a lower discharge capacity of 114 mAh·g^{-1}. For $Mg_{0.3}V_2O_5$, no obvious plateaus were observed on the charge–discharge curve and it had the lowest discharge capacity (91 mAh·g^{-1}). As can be seen in Figure 7c, $Mg_{0.3}V_2O_5 \cdot 1.1H_2O$ demonstrated good rate performance (50 mAh·g^{-1} at 4.0 A·g^{-1}) and high cycling stability (capacity retention of 80.0% after 10,000 cycles at 2.0 A·g^{-1}). In a full RMB cell with a $Na_2Ti_3O_7$ anode and the $Mg_{0.3}V_2O_5 \cdot 1.1H_2O$ cathode, the specific capacity of about 62 mAh·g^{-1} at the current density of 100 mA·g^{-1} was achieved, and the battery demonstrated a stable voltage plateau of 1.5 V and a cycle life of 100 cycles.

Mg^{2+}-pillared hydrated vanadium oxide $Mg_xV_5O_{12} \cdot nH_2O$ nanofibers (Figure 7d), with expanded interlayer spacing were obtained in [108]. Mg^{2+} pillars and structural H_2O molecules stabilized the material framework and promoted Mg^{2+} diffusion during cycling. At a current density of 0.05 A·g^{-1} the $Mg_xV_5O_{12} \cdot nH_2O$ electrode provided a high capacity of 160 mAh·g^{-1}, corresponding to 1.3 Mg^{2+} inserted per V_5O_{12} structural unit. The $Mg_xV_5O_{12} \cdot nH_2O$ electrode showed excellent long-term stability (81% capacity retention after 10,000 cycles at 2 A·g^{-1}), the coulombic efficiency was >99%. *In situ* XRD measurements (Figure 7e) had shown that the $Mg_xV_5O_{12} \cdot nH_2O$ electrode undergoes dynamic structural changes upon Mg^{2+}-intercalation/deintercalation. The (001) diffraction peak shifted to a higher angle region during the discharge process (reduction), indicating the gradual contraction of the interlayer spacing. During charging (oxidation), the (001) peak returned to the initial position by the end of a deep charge. The Mg^{2+}-intercalation caused a decrease in interlayer spacing to 1.10 nm, and it recovered to 1.19 nm upon Mg^{2+} deintercalation (Figure 7f,g).
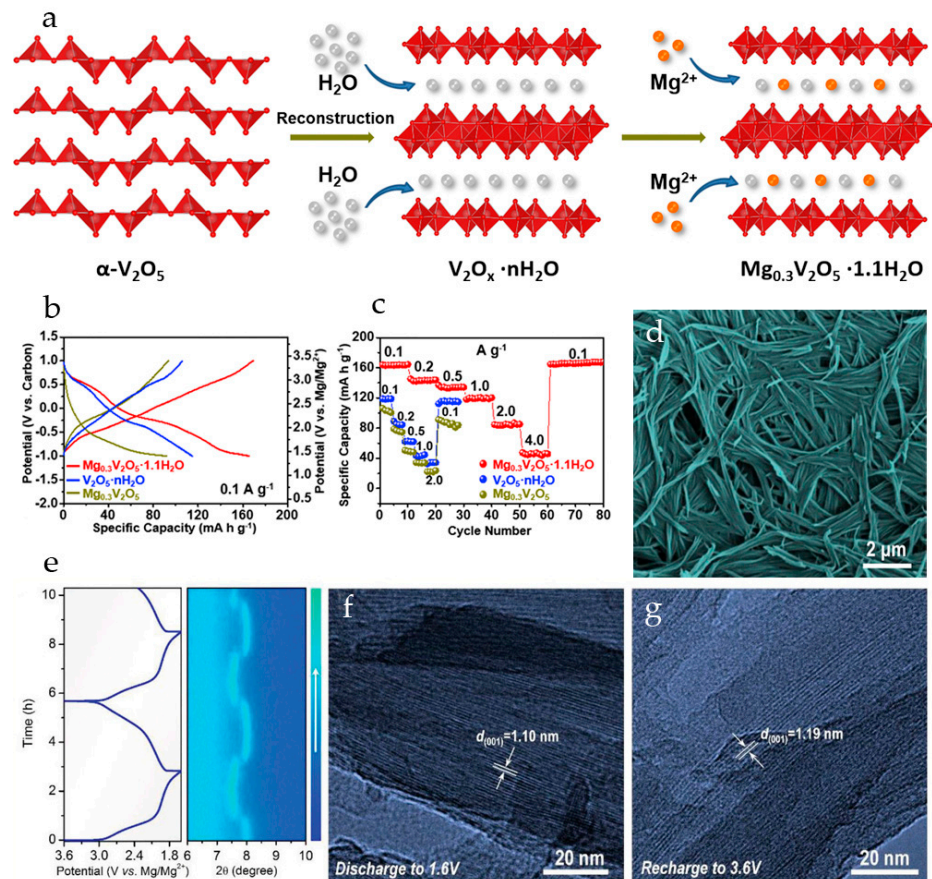
Figure 7. (**a**) Scheme of consecutive incorporation of water and magnesium to form the bilayer $Mg_{0.3}V_2O_5 \cdot 1.1H_2O$, (**b**) charge–discharge curves, and (**c**) rate performance of $Mg_{0.3}V_2O_5 \cdot 1.1H_2O$, $V_2O_5 \cdot nH_2O$, and $Mg_{0.3}V_2O_5$ (Reprinted with permission from [110]. Copyright 2019, Elsevier). (**d**) SEM image of MgVOH electrode, (**e**) *in situ* XRD contour map of the $Mg_xV_5O_{12} \cdot nH_2O$ electrode and corresponding high-resolution TEM images of (**f**) discharged and (**g**) recharged $Mg_xV_5O_{12} \cdot nH_2O$ electrode (Reprinted with permission from [108]. Copyright 2020, John Wiley and Sons).

Expanding the interlayer spacing of layered materials is an effective way to improve Mg^{2+}-ion storage performance. On the one hand, as the interlayer spacing increases, the interaction between intercalated guest ions and host lattices weakens, which greatly improves the mobility of cations in cathode materials. On the other hand, the number of available sites in cathode materials also increases due to the enlarged lattice spaces, leading to improved reversibility of Mg^{2+}-ion storage capacity.

2.6. Vanadium Oxides Pre-Intercalated with Organic Molecules and Conducting Polymers

The intercalation of conducting polymers into vanadium oxides has been shown to be advantageous for improving the functional properties of electrode materials. Conducting polymers intercalated into layered vanadium oxide can increase the interlayer spacing and stabilize the layered structures by reducing the coulombic interactions between the guest cations and the host framework, as has been shown on numerous examples for aqueous Zn-ion batteries [115].

Rechargeable magnesium batteries with a V_2O_5 xerogel cathode with polyethylene oxide (PEO) incorporated between the oxide layers showed a significant improvement in the reversible capacity of magnesium ions [116]. PEO was introduced in the V_2O_5 interlayer during the V_2O_5 sol–gel synthesis (Figure 8a,b); this approach allowed the expansion of the interlayer spacing in V_2O_5 and the reduction in the interaction of intercalated divalent Mg^{2+} with the host lattice. X-ray diffraction showed that the interlayer spacing in V_2O_5 xerogel was increased to 12.6–13.6 Å by the inclusion of PEO. Galvanostatic charge–discharge

profiles of V_2O_5 xerogel and V_2O_5-PEO nanocomposites with different amounts of PEO are shown in Figure 8c. In a cell with a Mg anode and a dry $Mg(ClO_4)_2/AN$ electrolyte, the V_2O_5-PEO-1 nanocomposite exhibited a discharge capacity of 100.3 $mAh \cdot g^{-1}$ at 10 $mA \cdot g^{-1}$, ~5 times higher than of V_2O_5 xerogel (and ~2 times higher than of V_2O_5-PEO-2), improved stability, and enhanced rate capability. The Mg^{2+}-ion capacity for the V_2O_5 xerogel, V_2O_5-PEO-1, and V_2O_5-PEO-2 cathode materials was determined as 0.06, 0.34, and 0.18 per V_2O_5 formula unit (i.e., x in $Mg_xV_2O_5$), respectively. In cyclic voltammograms, the V_2O_5-PEO-1 nanocomposite showed higher currents compared to V_2O_5 xerogel and V_2O_5-PEO-2, indicating that the introduction of an optimal PEO ratio within V_2O_5 improved the Mg ion charge storage performance. The Mg^{2+} diffusion coefficient in V_2O_5-PEO-1 nanocomposite was 4.7×10^{-11} $cm^2 \cdot s^{-1}$, that is, 2 times higher than the Mg^{2+} diffusion coefficient in the V_2O_5 xerogel. The Mg^{2+} diffusion coefficient in V_2O_5-PEO-2 was 2.5×10^{-12} $cm^2 \cdot s^{-1}$, lower than that for the V_2O_5 xerogel. Therefore, Mg^{2+}-ion diffusion was not only influenced by the interlayer spacing (which is the largest for V_2O_5-PEO-2), but also by the interlayer composition. It was suggested that a higher PEO ratio in the composite could result in lower charge storage for reasons such as a lower diffusion rate of Mg^{2+}-ions in PEO-rich regions, lower electronic conductivity due to the insulating nature of PEO, and coordination of PEO molecules with the V_2O_5 lattice, blocking sites for Mg^{2+} intercalation.
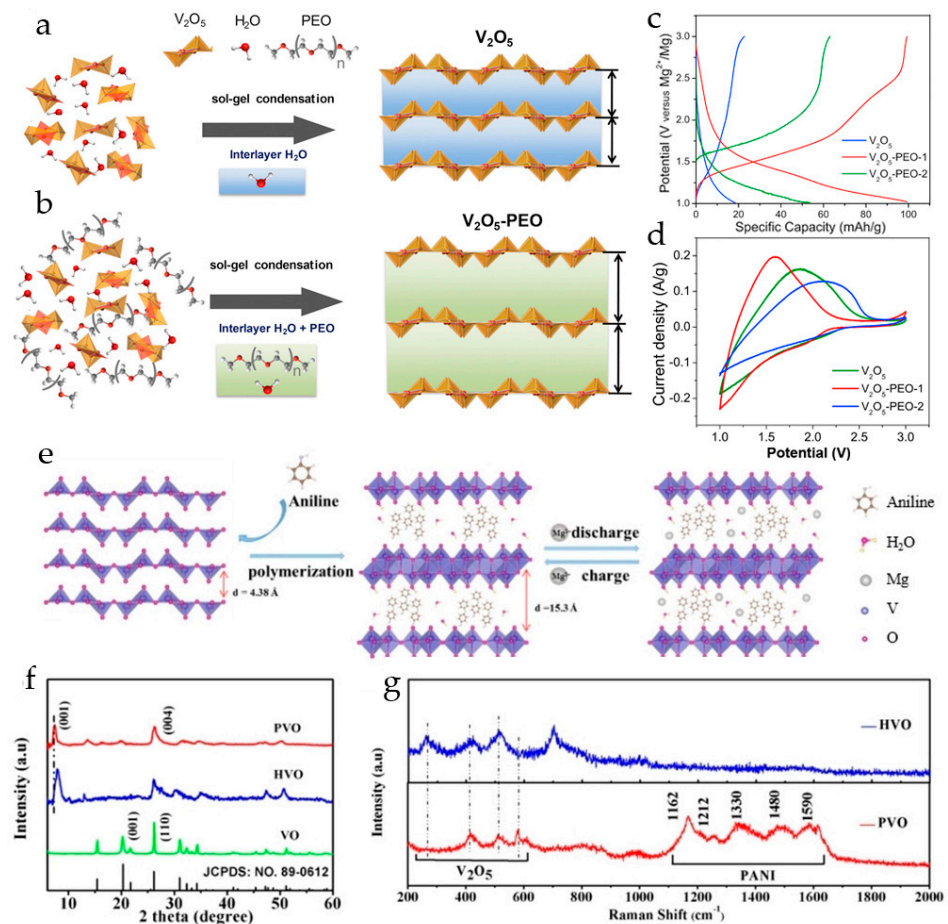
Figure 8. (**a**) Scheme of the growth of hydrated V_2O_5 nanosheets by condensation of $[VO_4]^{3-}$ polyanions in aqueous solution without PEO and (**b**) with PEO, (**c**) GCD profiles of V_2O_5, V_2O_5-PEO-1, and V_2O_5-PEO-2 at a current density of 10 $mA \cdot g^{-1}$, (**d**) cyclic voltammograms of V_2O_5, V_2O_5-PEO-1, and V_2O_5-PEO-2 at a scan rate of 2.5 $mV \cdot s^{-1}$. (Reprinted with permission [116]. Copyright 2017, Elsevier). (**e**) Scheme of the synthesis of the PVO superlattice, (**f**) XRD patterns of VO, HVO, and PVO, (**g**) Raman spectra of HVO and PVO. (Reprinted with permission [117]. Copyright 2021, John Wiley and Sons).

PANI-V_2O_5 2D organic–inorganic superlattices were synthesized and tested as cathode materials for RMBs in [117]. PANI-V_2O_5 (PVO) was synthesized via the intercalation of aniline monomers and subsequent interlayer polymerization (Figure 8e). In the acidic environment, the anilinium cations diffused into the interlayer space of V_2O_5 and underwent oxidative polymerization, V_2O_5 being a mild oxidizing agent. Compared to the XRD pattern of V_2O_5 (VO), a new diffraction peak of hydrated V_2O_5 (HVO) was located at 7.08°, confirming that the interlayer spacing of HVO is greater than that of VO, and for PVO, the new diffraction peak was shifted to a lower angle 6.47°, indicating larger interlayer spacing in PVO than in HVO and the insertion of PANI (Figure 8f). The formation of protonated PANI in PVO was confirmed by the Raman spectra (Figure 8g). PANI not only expanded the interlayer spacing of V_2O_5, but also provided additional charge storage sites. Benefitting from the above features, the PVO demonstrated high capacity (280 mAh·g^{-1} at a current density of 0.1 A·g^{-1}) and excellent rate performance (135 mAh·g^{-1} at a current density of 4 A·g^{-1}) in 0.3 M Mg(CF$_3$SO$_3$)$_2$/AN electrolyte. The PVO cathode delivered capacities of 275, 250, 220, 175, 155, and 130 mAh·g^{-1} at current densities of 0.1, 0.2, 0.5, 1.0, 2.0, and 4.0 A·g^{-1}, respectively. The PVO had an excellent cycling stability, and the retained capacity after 500 cycles at 4 A·g^{-1} was 80 mAh·g^{-1}.

Polyaniline was *in situ* intercalated into V_6O_{13} [118]. With the increase in the amount of aniline monomer, PANI-V_6O_{13} composites with different enlarged *d*-spacings (11.8, 13.4, and 14.7 Å) were obtained. The contents of V_6O_{13} and PA in the PA100-V_6O_{13} with 13.4 Å *d*-spacing were 88.18% and 9.60%, respectively. In the cell with an activated carbon anode and a Mg(TFSI)$_2$/DME electrolyte, the PA100-V_6O_{13} sample demonstrated the highest reversible capacity (195 mAh·g^{-1} at 0.1 A·g^{-1}), with a retention of 173 mAh·g^{-1} after 100 cycles. PANI-V_6O_{13} exhibited high rate capability (46 mAh·g^{-1} at 10 A·g^{-1}) and outstanding cycling stability (2500 cycles at 5 A·g^{-1}). The higher reversible capacity of Mg^{2+} storage of PA100-V_6O_{13} was mainly ascribed to the expanded interlayer spacing. The sample PA150-V_6O_{13} with a higher polyaniline content and a larger interlayer spacing had higher initial discharge capacity but less satisfactory cycling performance, probably due to poor structural stability which reduced the capacity retention. The Mg^{2+} diffusion coefficients in PANI-V_6O_{13} calculated from GITT data varied over the entire insertion/extraction processes and were in the range from 2.1×10^{-9} to 7.5×10^{-12} and from 2.7×10^{-10} to 3.2×10^{-11} for the insertion and extraction processes, respectively. Thus, in polyaniline-intercalated V_6O_{13}, the Mg^{2+} intercalation kinetics were enhanced due to the π-conjugated polyaniline molecules weakening strong coulombic interactions between Mg^{2+}-ions and anions in the host material.

The layered V_2O_5-PEDOT composite with an enlarged interlayer spacing of 9.86 Å was synthesized in [119] via *in situ* polymerization of 3,4-ethylenedioxythiophene and sequential intercalation of PEDOT and cetyltrimethylammonium bromide (CTAB) into V_2O_5. In the XRD pattern of the as-prepared V_2O_5-PEDOT (VOP), a new peak appears at 8.96°, corresponding to an increased interlayer spacing of 9.86 Å, much larger than the *d*-spacing of V_2O_5 (4.38 Å). The intercalation of PEDOT pillars results in dark coloring of the VOP powder; these pillars change the structure of bulk V_2O_5 by drastic volume expansion, resulting in delamination of the VOP into a nest-like structure of interlaced nanowires about 50 nm in diameter, as seen in the SEM image (Figure 9a–c). The magnesium storage performance of V_2O_5-PEDOT cathode was evaluated in a cell with a Mg anode and all-phenyl complex APC-CTAB/THF electrolyte. The CTAB was added for further improvement in the Mg^{2+} diffusion kinetics. Two pairs of broad redox peaks located at around 1.25/0.80 and 1.78/1.57 V (vs. Mg/Mg^{2+}) were observed in the cyclic voltammograms of V_2O_5-PEDOT. The reversible capacity of V_2O_5-PEDOT in the full cell was 288.7 mAh·g^{-1} at 0.1 A·g^{-1}, and the electrode demonstrated high cyclability (over 500 cycles at 0.5 A·g^{-1} with capacity retention 68%).
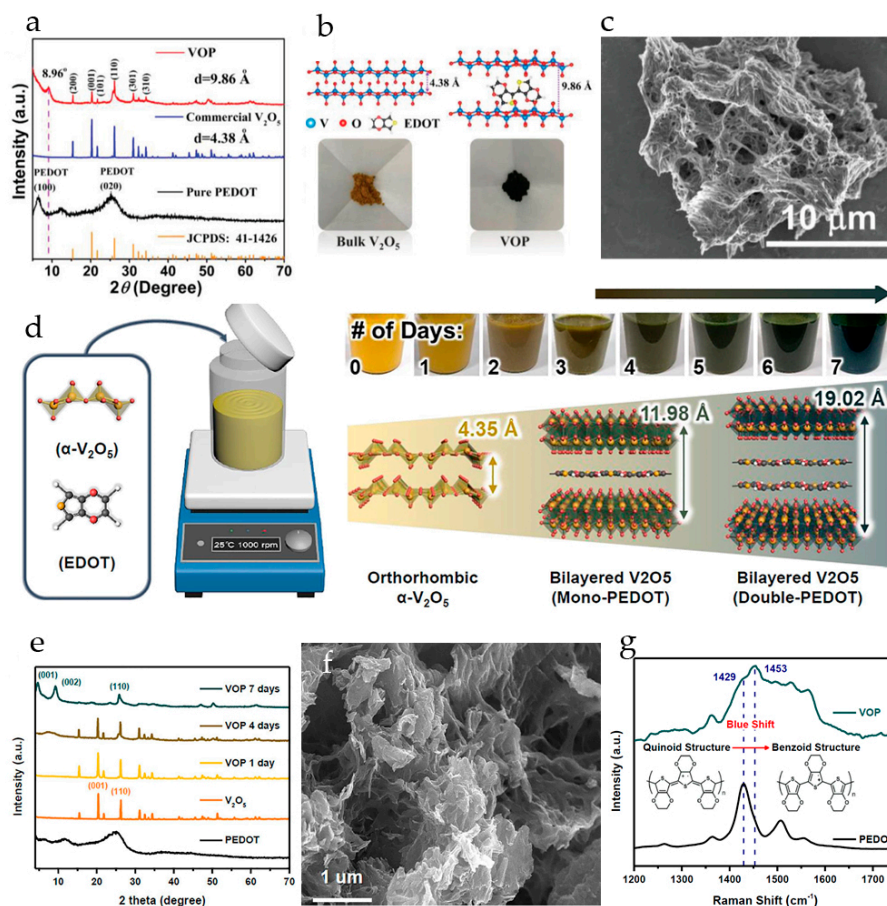
Figure 9. (**a**) XRD patterns of PEDOT, commercial V_2O_5 and as-prepared VOP composite, (**b**) schematic structure and optical images of commercial V_2O_5 and VOP composite, (**c**) SEM image of VOP composite. (Reprinted with permission [119]. Copyright 2021, John Wiley and Sons). (**d**) Schematic representation of the VOP synthesis, (**e**) XRD patterns of pristine V_2O_5, PEDOT, and as-prepared VOP, (**f**) SEM of VOP, (**g**) Raman spectra of PEDOT and blue-shifted VOP. (Reprinted with permission [120]. Copyright 2023, Elsevier).

A V_2O_5/PEDOT (VOP) composite was synthesized by intercalating poly-3,4-ethylenedioxythiophene into V_2O_5 under stirring at room temperature for 1 week (Figure 9d) [120]. After 4 days of stirring, a new diffraction peak appeared in the XRD pattern of VOP at 7.6°, corresponding to an interlayer spacing of 11.98 Å. After 7 days of stirring, two new peaks appeared at 4.65° and 9.32°, corresponding to an interlayer spacing of 19.02 Å of the (001) plane and 9.49 Å of the (002) plane (Figure 9e). It was observed that the bilayer structure of orthorhombic V_2O_5 was retained even after the insertion of PEDOT. The porous structure of the as-prepared VOP resulting from the aggregation of the bilayer structures is shown in the SEM image (Figure 9f). The electronic coupling of PEDOT with V_2O_5 interlayers led to a change in PEDOT structure from the quinoid to the benzoid, and the corresponding blue shift of the principal peaks of PEDOT was observed in UV-vis spectra (Figure 9g). A reversible and fast Mg^{2+} ion insertion/extraction in/out of an enlarged interlayer spacing of 19.02 Å (in the charged state at +1.0 V) and 20.16 Å (in the discharge state at −1.0 V) was achieved. The VOP electrodes in 0.3 M $Mg(TFSI)_2$/AN delivered a high specific capacity of 339.7 mAh·g^{-1} at 0.1 A·g^{-1}, high rate capacity of 256.3 mAh·g^{-1} at 0.5 A·g^{-1}, and long-term cyclic stability with a 0.065% decay rate and high capacity of 172.5 mAh·g^{-1} after 500 cycles. VOP delivered much higher specific capacities (320, 271, 220, 172, and 117 mAh·g^{-1}) than pristine V_2O_5 (72.0, 67, 58, 50, and 43 mAh·g^{-1}) at the current densities of 0.1, 0.2, 0.5, 1.0, and 2.0 A·g^{-1}, respectively. The enhancing effect of water activation on the kinetics was confirmed. When 3 M H_2O was added to

0.3 M $Mg(TFSI)_2$/AN, the discharge capacities of VOP at 0.1 $A \cdot g^{-1}$ increased from 165 to 348 $mAh \cdot g^{-1}$, and the capacity of pristine V_2O_5 increased from 82 to 113 $mAh \cdot g^{-1}$. The improvement in the electrochemical performance of VOP and pristine V_2O_5 was attributed to the lowered desolvation energy of the solvated Mg^{2+}-ions.

$V_2O_5 \cdot H_2O$ was synthesized and intercalated with polyacrylonitrile (PAN) by hydrothermal synthesis procedure [121]. The exact chemical composition of the PAN-intercalated oxide was $V_2O_5 \cdot 0.34H_2O$-PAN, and that of vanadium oxide used for comparison was $V_2O_5 \cdot 0.33H_2O$. According to XRD data, all peaks of the V_2O_5-PAN and $V_2O_5 \cdot H_2O$ were consistent with double-layer V_2O_5 (JCPDS No. 40-1296). The layer spacing increased from 9.91 Å in the pure $V_2O_5 \cdot H_2O$ to 10.63 Å in V_2O_5-PAN. It was shown that intercalation of PAN also induced cation reduction and generated abundant anion vacancies, thus improving ion diffusion and electron transfer kinetics. V_2O_5-PAN electrodes had perfect structural stability and electrochemical reversibility during charge–discharge. After stabilization, V_2O_5-PAN achieved a high specific discharge capacity of ~180 $mAh \cdot g^{-1}$ at 50 $mA \cdot g^{-1}$ in 0.5 M $Mg(TFSI)_2$/AN electrolyte, and its life-span at 2 $A \cdot g^{-1}$ was 18,000 cycles.

The general tendency of positive effects observed with the introduction of conducting polymer molecules is explained by the formation of "pillars" expanding the interlayers, and also by the improvement in electrical conductivity and the effect of electrostatic shielding of the host from the high charge density of Mg^{2+}. However, to date, the role of the composition/nature and the optimal fraction of conducting polymers introduced into the layered structure need further investigation.

3. Mechanisms of Intercalation and Role of Structural Water

The general operating principle of RMBs in dry aprotic electrolytes is thought to be similar to that of other metal ion batteries. It is based on the reversible intercalation/deintercalation of Mg^{2+}-ions into the active material of the cathode. However, there is some controversy in the studies of the mechanism of Mg^{2+} intercalation in dry electrolytes; the reaction mechanism of α-V_2O_5 in RMBs with a dry electrolyte is not well understood.

A systematic study of Mg insertion into orthorhombic V_2O_5 was performed by combining electrochemical and structural methods [122]. The results for an electrochemically cycled V_2O_5 cathode in a full cell with Mg metal anode obtained by atomic-resolution transmission electron microscopy showed the local formation of the theoretically predicted ε-$Mg_{0.5}V_2O_5$ phase; however, the intercalation level of Mg was low.

The investigations of the electrochemical behavior of orthorhombic α-V_2O_5 in dry and "wet" alkyl carbonate-based electrolytes and the insertion-driven structural changes of the active phase studied by *ex situ* X-ray diffraction showed that proton intercalation dominates the reaction of α-V_2O_5, even in a dry electrolyte, and the intercalation of Mg^{2+}-ions is negligible [123].

In operando studies of the reaction mechanism of α-V_2O_5 cathodes in RMBs by synchrotron diffraction and *in situ* X-ray absorption near-edge spectroscopy (XANES) together with *ex situ* Raman and X-ray photoelectron spectroscopy [75] have shown the reversibility of magnesium ion intercalation and provided information on the evolution of the crystal structure and the change in oxidation degrees during charge–discharge cycling. It was shown that α-V_2O_5 transforms to a Mg-poor phase ($Mg_{0.14}V_2O_5$) during discharging, and then undergoes a two-phase transition.

There are three related issues, the role of which in the case of vanadium oxide cathodes for RMBs should be considered in more detail:

(i) Crystalline V_2O_5 is capable of reversible intercalation of Mg^{2+} in "wet" organic electrolytes, containing enough water molecules to coordinate to Mg^{2+}-ions and shield their high charge during intercalation, thus allowing faster diffusion of Mg^{2+}-ions within the host material.

(ii) The incompatibility of metallic Mg anodes with wet electrolytes leads to the focus of the research on the bilayer V_2O_5, hydrated, and water-pillared vanadium oxides, where water molecules are naturally present in the lattice [104,108,111]. The interlayer

water molecules effectively shield the interaction between Mg^{2+} and the host lattice, improving the reversibility of Mg^{2+}-ion intercalation/deintercalation and structural stability of the cathode material during cycling.

Following the pioneering work [61], many researchers noted that V_2O_5 exhibits improved capacity in aprotic electrolytes containing small amounts of water. In particular, the study of the electrochemical performance of V_2O_5 cathodes in $Mg(ClO_4)_2$/PC and $Mg(TFSI)_2$/G2 electrolytes [124,125] showed that controllable amounts of water lead to increased specific capacities.

Water molecule intercalation into V_2O_5 structures improves Mg^{2+}-ion diffusion kinetics due to enlarged interlayer spacing. In addition, the water molecules in the cathode increase electrostatic shielding, which is a very important factor for improving the migration rate of Mg^{2+}-ions within the host material [47,124].

The experimental observations of the positive influence of water molecules in non-aqueous electrolytes on the charge storage properties of V_2O_5 (higher currents in CVs, higher capacities, lower polarization) were later extended by the experimental results pointing to the mechanism in which both protons and magnesium ions participate as charge carriers in the redox process.

Some works demonstrate co-intercalation of protons together with magnesium ions, providing higher capacity of vanadium oxide cathodes. A number of works demonstrate the dominant role of reversible proton insertion in the capacity of RMB in aqueous electrolytes and non-aqueous electrolytes containing small amounts of water.

The study of the influence of water additive in the organic electrolyte had shown that the presence of water enables higher capacities for an α-V_2O_5 cathode [125]. The capacity achieved for the wet electrolyte was ~260 mAh·g^{-1}, which is close to the theoretical value. In dry electrolyte, a discharge capacity of only ~60 mAh·g^{-1} was achieved. Solid state NMR revealed that the major contribution towards the higher capacity in high water-containing electrolyte solution (1 M $Mg(TFSI)_2$/G2 with 2600 ppm H_2O) originates from the reversible proton insertion. On lowering the water level of the electrolyte (1 M $Mg(TFSI)_2$/G2 with 15 ppm H_2O), the evidence of reversible Mg intercalation was obtained by EDX of the discharged V_2O_5, which demonstrated the presence of a higher concentration of Mg in the discharged state compared to the charged and pristine V_2O_5 electrodes.

The intercalation of Mg^{2+} in α-V_2O_5 was again investigated in dry and water-containing organic electrolytes [126]. An improved electrochemical performance was observed after adding water to a dry organic electrolyte; this effect was explained by the co-intercalation of protons and Mg^{2+}. The discharged product of α-V_2O_5 in a 0.5 M $Mg(ClO_4)_2$ + 2.0 M H_2O/AN electrolyte was $Mg_{0.17}H_xV_2O_5$ (x = 0.66–1.16), indicating that the capacity is mainly due to proton intercalation.

The magnesium ion storage capability of a VO_2(B) cathode in dry and wet 0.5 M $Mg(ClO_4)_2$/AN electrolytes was studied in [56]. The water content in dry and wet electrolytes was 40 and 650 ppm, respectively. In the dry electrolyte, VO_2(B) deliveredan initial discharge capacity of 50.6 mAh·g^{-1} at a current density of 20 mA·g^{-1}, with a coulombic efficiency of 94.4%. Under the same electrochemical test conditions, the initial discharge capacity of VO_2(B) in the wet electrolyte was 251.0 mA·g^{-1}, with a coulombic efficiency of 99.4%. The high discharge capacity observed in the wet electrolyte was attributed to predominant proton intercalation instead of magnesium intercalation. It was also shown that VO_2(B) may suit as a high-performance cathode material only if its particles are relatively small, to exclude long distances for Mg^{2+}-ion diffusion along the diffusion channels within the material.

The strongly polarizing nature of Mg^{2+}-ions leads to slow intercalation kinetics. The structural water in host electrode materials facilitates migration of Mg^{2+}-ions due to the "lubricating" effect; in addition, water molecules act as charge screening media to reduce the coulombic repulsion between the ions and the host lattice.

The enhanced insertion reaction of Mg^{2+}-ions into the $V_2O_5(H_2O)_y$ (2 < y < 3) xerogel, containing single and/or double layers of H_2O molecules in the interlayer space of the

oxide, was reported as early as 1992 in [127]. Bonded H_2O molecules allowed smooth insertion and de-insertion of Mg^{2+}-ions during the electrochemical cycling of V_2O_5 xerogel electrodes in a dry 1 M $Mg(ClO_4)_2$/AN electrolyte. The specific charge density 170 $Ah \cdot kg^{-1}$ was measured in the first cycle for V_2O_5 xerogel, while less than 50 $Ah \cdot kg^{-1}$ was observed in the first cycle for pure V_2O_5.

Layered $H_2V_3O_8$ nanowires demonstrated high Mg^{2+}-ion storage with a capacity of 304.2 $mAh \cdot g^{-1}$ at 50 $mA \cdot g^{-1}$ in a three-electrode cell with 0.5 M $Mg(ClO_4)_2$/AN electrolyte and activated carbon cloth as counter and reference electrodes [128]. In the cyclic voltammograms at a scan rate of 0.2 $mV \cdot s^{-1}$, one cathodic peak at ~2.0 V and two anodic peaks at 2.3 and 2.5 V (vs. Mg/Mg^{2+}) were observed, which were ascribed to the insertion and extraction of magnesium ions. GCD curves showed that $H_2V_3O_8$ nanowires possess a high working voltage platform of about 2.0 V. $H_2V_3O_8$ nanowires demonstrated 85.9% capacity retention after 20 cycles at 50 $mA \cdot g^{-1}$.

Hydrated vanadium oxide $H_2V_3O_8$ nanowires were synthesized via a one-step hydrothermal method [129]. The $H_2V_3O_8$ nanowires had a diameter of 100–200 nm (Figure 10a,b) and an interlayer spacing of 0.34 nm (Figure 10c), corresponding to the d(011) spacing of $H_2V_3O_8$. The material exhibited reversible magnesiation/demagnesiation with an initial discharge capacity of 80 $mAh \cdot g^{-1}$ and 231 $mAh \cdot g^{-1}$ at 10 $mA \cdot g^{-1}$ at 25 °C and 60 °C, respectively (Figure 10d), and an average discharge voltage of ~1.9 V (vs. Mg/Mg^{2+}) in a dry (48 ppm H_2O) 0.5 M $Mg(ClO_4)_2$/AN electrolyte. The discharge capacities of $H_2V_3O_8$ at 60 °C were 231, 201, 170, and 97 $mAh \cdot g^{-1}$ at the current densities of 10, 20, 40, and 80 $mA \cdot g^{-1}$, respectively (Figure 10e). The capacity observed at 25 °C in dry electrolyte was much lower than the value of 304.2 $mAh \cdot g^{-1}$ reported for $H_2V_3O_8$ in [128] due to the difference in the water content in the organic electrolyte. In the wet electrolyte (5790 ppm H_2O), it increased to ~260 $mAh \cdot g^{-1}$. The structural water of $H_2V_3O_8$ ($V_3O_7 \cdot H_2O$) remained stable during cycling. The chemical formula for the discharged electrode at 60 °C was calculated as $Mg_{1.22}H_2V_3O_8$, considering that one electron charge transfer corresponds to 94.75 $mAh \cdot g^{-1}$ per formula unit of $H_2V_3O_8$. The analysis of the discharged electrode suggested the chemical formula $Mg_{0.97}H_2V_3O_8$ (Figure 10f). The difference of ~20% was explained by the thorough washing of the electrodes during the sample preparation for elemental analysis, when the bulk-intercalated Mg^{2+}-ions remained and the surface ions were washed out. A homogeneous distribution of Mg^{2+}-ions was observed in the vanadium oxide particles of the discharged electrode, while they were absent in the initial or charged samples (Figure 10 g–i).

It was shown that the kinetic and the electrochemical properties of $H_2V_3O_8$ (HVO) are improved by adding water to a dry organic electrolyte [130]. HVO nanofibers were synthesized by exfoliation of V_2O_5 followed by a hydrothermal process. $H_2V_3O_8$ delivered an initial specific capacity of 303 $mAh \cdot g^{-1}$ at a current density of 50 $mA \cdot g^{-1}$ in a wet $Mg(ClO_4)_2 \cdot 3.1H_2O$/AN electrolyte, four times higher than in a dry electrolyte (67 $mAh \cdot g^{-1}$). Although the presence of water in the aprotic electrolyte was beneficial for the specific capacity, the capacity retention in the wet electrolyte was 80% after 30 cycles at 50 $mA \cdot g^{-1}$ and 61% after 200 cycles at 100 $mA \cdot g^{-1}$, while in the dry electrolyte the capacity retention was 99% after 30 cycles at 50 $mA \cdot g^{-1}$ and 109% after 200 cycles at 100 $mA \cdot g^{-1}$, demonstrating the long-term stability and the reversibility of the charge–discharge process in the dry electrolyte. In an "ambient" $Mg(ClO_4)_2 \cdot 1.4H_2O$/AN electrolyte, the HVO cathode delivered an initial specific capacity of 167 $mAh \cdot g^{-1}$ at a current density of 50 $mA \cdot g^{-1}$ and showed a capacity retention of 73% after 30 cycles, suggesting that the water content in the electrolyte affects the reversibility of the charge–discharge processes. The structural changes in HVO as a function of the water content in the electrolyte were studied by *in operando* XRD during galvanostatic cycling. It was observed that the HVO structure almost fully recovered after two discharge/charge cycles in dry electrolyte, while in the presence of water, irreversible changes in the lattice parameters occurred in the initial cycle followed by a reversible discharge/charge cycle. In the presence of water, the changes in lattice parameters and unit cell volume during discharge/charge were 8 times larger, supporting

the hypothesis that H_2O molecules from a hydration shell co-intercalate with Mg^{2+} ions, thus leading to a decrease in the cycling stability of HVO in electrolytes with water content. In the wet and "ambient" electrolytes, the insertion of ~0.60 equivalent Mg^{2+} into HVO took place. In the wet electrolyte, STEM/EDX (Figure 10 j–m) revealed that the inserted Mg^{2+}-ions were mainly accumulated close to the surface and at the edges of the HVO fibers, but did not diffuse into the bulk. This explained the high reversibility of the insertion process and the small lattice parameter changes.
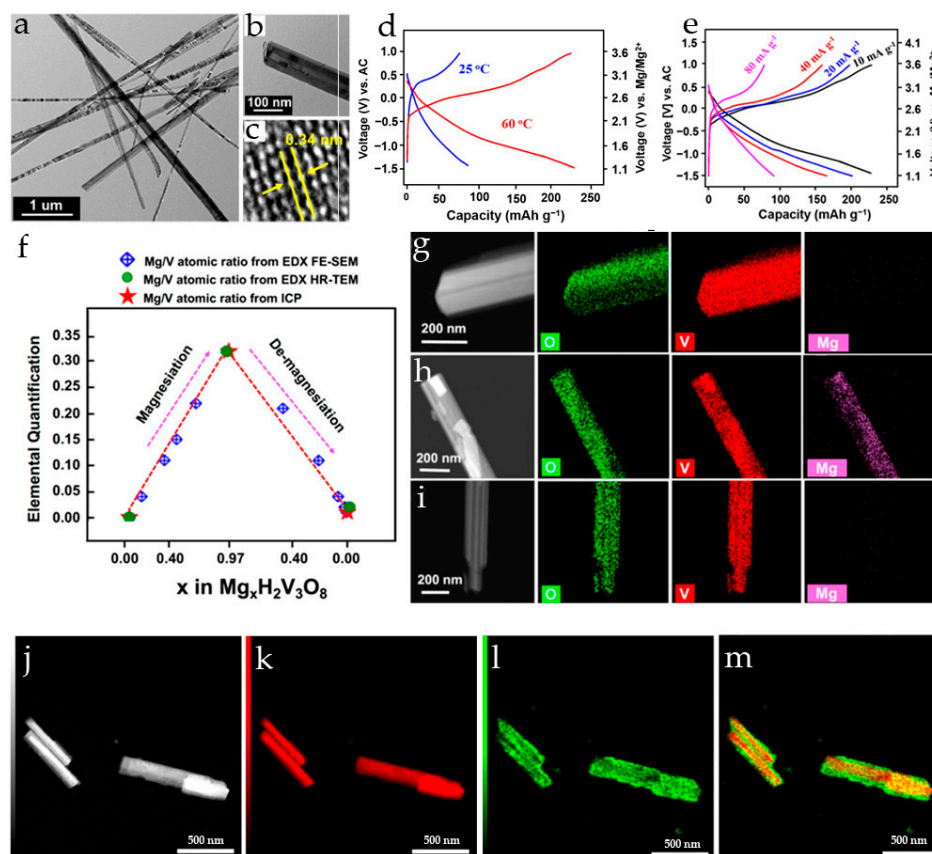
Figure 10. (**a**,**b**) TEM images of $H_2V_3O_8$ nanowires, (**c**) HR-TEM image of $H_2V_3O_8$ nanowires, (**d**) initial GCD profiles of $H_2V_3O_8$ in 0.5 M $Mg(ClO_4)_2$/AN at 25 and 60 °C at a current density of 10 mA·g^{-1}, (**e**) initial GCD profiles $H_2V_3O_8$ at 60 °C at various current densities, (**f**) Mg/V atomic ratios for $Mg_xH_2V_3O_8$ electrodes during the discharge–charge cycle, (**g**) FE-TEM EDX elemental mapping of initial (x = 0) electrode, (**h**,**i**) FE-TEM EDX elemental mapping of discharged (x = 0.97), and charged (x = 0) electrodes. (Reprinted with permission from [129]. Copyright 2018, American Chemical Society). (**j**) HAADF STEM image of HVO nanofibers cycled in wet electrolyte, (**k**,**l**) corresponding V-K edge and Mg-K edge EDX intensity maps, (**m**) overlay of V-K and Mg-K edge EDX intensity maps. (Reprinted with permission from [130]. Copyright 2022, Elsevier).

Introducing water molecules into the lattice material together with cation pre-intercalation is also an effective strategy for improving the electrochemical performance of V_2O_5 in RMBs. Mn^{2+}-ions were introduced into the hydrated vanadium oxide by a hydrothermal method in [111]. The experimental results revealed the synergetic effect of both Mn^{2+} ions and crystal water in the $Mn_{0.04}V_2O_5·1.17H_2O$ nanobelts, improving the structural and cycle stability of the cathode in the $Mg(TFSI)_2$/AN electrolyte. The $Mn_{0.04}V_2O_5·1.17H_2O$ material exhibited a high specific capacity (145 mAh·g^{-1} at 50 mA·g^{-1}), good rate capability (50 mAh·g^{-1} at 4 A·g^{-1}), and long cycle stability (82% capacity retention after 10,000 cycles at 2 A·g^{-1}), better than that of water-free $Mn_{0.04}V_2O_5$. The *in situ* and *ex situ* material

characterizations revealed that the structure of $Mn_{0.04}V_2O_5 \cdot 1.17H_2O$ was stable during the charge–discharge process.

Water-lubricated and aluminum ion-pillared vanadate $H_{11}Al_2V_6O_{23.2}$ (HAlVO) was reported as a high-performance cathode material for Mg^{2+} ion storage [113]. The capacity fade mechanism of water-free aluminum vanadate AlV_3O_9 (AlVO) was also investigated. The charge transfer process in water-lubricated and water-free aluminum vanadates was analyzed by DFT calculations, and the different charge transfer processes in the two materials and the charge shielding effect of the water molecule in HAlVO were revealed. The comparison of the cyclic voltammograms of HAlVO and AlVO showed that the shape of the CVs and the position of the redox peaks of the two materials are different: HAlVO had more intense reduction and oxidation peaks than AlVO (Figure 11a). HAlVO displayed higher initial specific capacity and a more stable cycle performance (165 mAh·g^{-1} in the 1st and 50th cycles), while AlVO exhibited a capacity of only 125 mAh·g^{-1} in the 1st cycle, which decreased to 105 mAh·g^{-1} in the 50th cycle (Figure 11b,c). Water-lubricated HAlVO had better cycle performance at all current densities. The diffusion coefficients were obtained for HAlVO and AlVO from GITT curves at different stages of Mg^{2+} insertion. At the initial stage of Mg^{2+} insertion, D_{HAlVO} was 4.45×10^{-11} cm^2·s^{-1} and D_{AlVO} was 2.77×10^{-11} cm^2·s^{-1}. When the amount of inserted Mg^{2+} reached 100%, D_{HAlVO} decreased to 1.01×10^{-11} cm^2·s^{-1} and D_{AlVO} to 2.12×10^{-12} cm^2·s^{-1}. The faster decrease in the diffusion rate of Mg^{2+} in AlVO than in HAlVO was explained by larger interlayer spacing of HAlVO and the shielding effect of interlayer water molecules, providing more active storage sites for Mg^{2+}, enough diffusion space, and less charge repulsion when a large amount of Mg^{2+}-ions is intercalated into HAlVO. The scheme of reversible insertion/extraction of Mg^{2+} in HAlVO is shown in Figure 11d. Pre-intercalated Al^{3+} ions act as "pillars" which stabilize the V-O layered structure both in discharged and charge states, which improves the cyclic stability of the electrode. When Mg^{2+} ions are inserted, the water molecules in the interlayer space facilitate achieving local electroneutrality and a lower Mg diffusion barrier; this improves the rate performance of HAlVO. The DFT calculation results suggested that the water molecules also reduce the insertion energy barrier of Mg^{2+}, thus improving the specific capacity of HAlVO. The charge transfer occurs mainly from the Mg^{2+} to O of the water molecule, and less from Mg^{2+} to O in the V-O layer, thus probably preventing the structural decay of the cathode during cycling.

A Mg^{2+} pre-intercalated hydrated $V_{10}O_{24} \cdot nH_2O$ layered material was obtained [107]. $Mg_{0.75}V_{10}O_{24} \cdot 4H_2O$ (MVOH) had an interlayer spacing of 13.9 Å, much larger than that of the hydrated $Mg_xV_5O_{12}$ (11.9 Å) reported in [108]. The nanoflower morphology greatly increased the specific surface area of the MVOH (33.07 m^2·g^{-1}) and provided short diffusion paths for Mg^{2+} from bulk solution to active sites, accelerating the insertion/extraction of Mg^{2+}. The diffusion coefficient of Mg^{2+} in the MVOH calculated from the EIS data was as high as 1.08×10^{-9} cm^2·s^{-1}, indicating fast migration kinetics inside the MVOH crystal lattice. In a three-electrode cell with a platinum counter electrode, a saturated calomel reference electrode (SCE), and 2 M $Mg(CF_3SO_3)_2$ aqueous electrolyte, the MVOH cathode exhibited a high discharge capacity of 350 mAh·g^{-1} (at 0.05 A·g^{-1}) and 70 mAh·g^{-1} at a higher current density of 4 A·g^{-1}. The full cell with a MVOH cathode, perylene-3,4,9,10-tetracarboxylic dianhydride (PTCDA) as an anode, and 2 M $Mg(CF_3SO_3)_2$ in PEG/H_2O (1:1) electrolyte, delivered a discharge capacity of 133 mAh·g^{-1} at a current density of 0.02 A·g^{-1} and 42 mAh·g^{-1} at a high current density of 4 A·g^{-1}, demonstrating high rate capability and satisfactory cycling stability with a capacity retention of 62% after 5000 cycles at 4 A·g^{-1}. DFT calculations performed on the basis of structural characterization results demonstrated that pre-intercalated Mg^{2+}-cations and structural H_2O molecules stabilize the layered structure of MVOH. Based on the determined pre-intercalated structure of MVOH, DFT calculations were performed to identify the energetically favorable sites for Mg^{2+} to occupy and the nearest neighboring site for Mg^{2+} to hop to. Based on the relaxed structures, the waltz-like like shuttle mechanism of H_2O molecules coordinated with Mg^{2+} transport was demonstrated during the charge–discharge of the MVOH cathode. It was shown

that the Mg^{2+}-ion migrates together with the coordinated water molecules, which adjust their orientation by rotating or flipping to facilitate the zig-zag migration of Mg^{2+}-ions (Figure 11e). After the extraction of Mg^{2+} from MVOH, the Mg^{2+}-H_2O bonds break, and the lattice H_2O molecules rearrange and form H-bonds in the interlayer of MVOH to stabilize the lamellar structure. To verify the Mg^{2+} shuttling of lattice H_2O molecules, the MVOH cathode was investigated by *in situ* Raman spectroscopy during discharging/charging, and a variation in the peak at 871 cm^{-1}, corresponding to the V-OH$_2$ bonds, at different discharged/charged states, was observed (Figure 11f). To further verify the Mg^{2+} shuttle function of lattice H_2O molecules, the fully discharged and charged MVOH cathode was analyzed by time of flight–secondary ion mass spectrometry (TOF-SIMS). The much higher intensity of the $MgVO^-$ signal in the discharged MVOH than in the charged MVOH indicates successful insertion of Mg^{2+} during discharge, and the higher $MgOH^+$ signal in the discharged MVOH than in the charged MVOH indicates strong coordination of lattice H_2O molecules with Mg^{2+}-ions inserted during discharge, confirming the H_2O–Mg^{2+} shuttle mechanism. The same intensity and distribution of the H^+ signal in discharged and charged MVOH indicate that the H_2O-Mg^{2+} waltz-like shuttle mechanism eliminates the co-insertion or co-extraction of H^+ together with Mg^{2+} (Figure 11g–i).
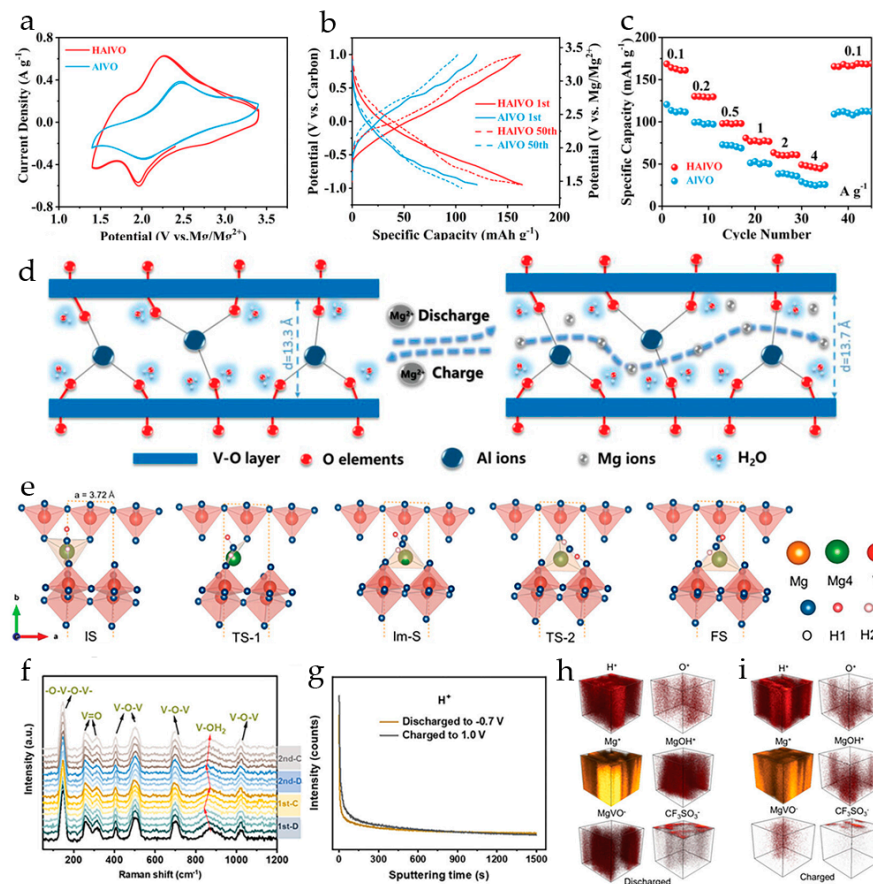
Figure 11. (**a**) The first two CVs of HAlVO and AlVO at the scan rate of 1 mV·s^{-1}, (**b**) the first and fiftieth charge and discharge curves of HAlVO and AlVO at the current density of 100 mA·g^{-1}, (**c**) rate performance of HAlVO and AlVO at the current densities of 0.1–4.0 A·g^{-1}, (**d**) schematic of the reversible insertion/extraction of Mg^{2+} ions in water-lubricated HAlVO. (Reprinted with permission from [113]. Copyright 2022, John Wiley and Sons). (**e**) Migration of Mg^{2+} ions along the *a* direction in the interlayer of MVOH during the H_2O-Mg^{2+} waltz-like shuttle, (**f**) *in situ* Raman spectra of the MVOH cathode at different discharge/charge states, (**g**) depth profile of H^+, (**h,i**) TOF-SIMS imaging of H^+, O^+, Mg^+, $MgOH^+$, $MgVO^-$, and $CF_3SO_3^-$ in fully discharged and charged electrode [107].

To sum up, the investigations of vanadium oxide-based cathodes in RMBs show that the water content, even in trace amounts, has an important influence on the mechanism of intercalation processes in organic electrolytes. Although the exact mechanism of the effect of the water molecules present in organic electrolytes on the increase in the specific capacity of vanadium oxide-based cathodes is not fully understood, it has been emphasized by many researchers. The following explanations have been proposed:

(i)   Water molecules can solvate the magnesium ions and shield their divalent charge to facilitate insertion into the interlayer spaces of VO-based cathodes.

(ii)   Water molecules inserted together with magnesium ions solvate the interstitial space and inner -V=O groups, and can lubricate Mg^{2+} diffusion.

(iii) Insertion or co-insertion of protons (from water molecules) takes place.

(iv)   Water molecules can react with the surface -V=O groups to form stable structural hydroxyl groups to reduce the migration barrier of magnesium insertion.

A better understanding of these effects is also necessary for the proper design of compatible cathodes and electrolytes.

For more illustrative comparison, the main electrochemical characteristics of selected vanadium oxide-based cathode materials are listed in Table 2.

Table 2. Summary of electrochemical performance of selected vanadium oxide-based cathodes in RMBs.

Cathode Material	Synthesis Method	Morphology/ Interlayer Spacing, Å	Electrolyte	Specific Capacity, mAh·g^{-1} (Current Density, A·g^{-1})	Capacity Retention (Number of Cycles and Current, A·g^{-1})	Ref.
V_2O_5 thin film	vacuum deposition	200 nm film	0.5 M Mg(ClO$_4$)$_2$/AN	180 (0.15 mV·s^{-1})	83% (36, 0.15 mV·s^{-1})	[71]
α-V_2O_5	commercial product	powder	1 M Mg(TFSI)$_2$/G2, 15 ppm H$_2$O	80 (20 µA·cm^{-2}), initial 60 (20 µA·cm^{-2})	94% (2–10, 0.05)	[125]
α-V_2O_5	commercial product	powder	1 M Mg(TFSI)$_2$/G2, 2600 ppm H$_2$O	250 (20 µA·cm^{-2})	-	[125]
α-V_2O_5	commercial product	powder	0.5 M Mg(TFSI)$_2$/PY$_{14}$TFSI, at 110 °C	295 (C/5)	83.8% (50, C/5)	[72]
α-V_2O_5	precipitation, calcination	spheres/11.52	0.2 M Mg(ClO$_4$)$_2$/AN	225.0 (0.01), initial 190 (0.01) 100 (0.03) 55 (0.05) 40 (0.08)	95% (50, 0.05) 87% (100, 0.05)	[77]
V_2O_5 film	AACVD	thin film	0.075 M MgCl$_2$	427 (5.9) 170 (2.4)	82% (2000, 5.9)	[73]
V_2O_5·nH$_2$O	ion-exchange	bilayered	1 M Mg(TFSI)$_2$/G2	50 (20 µA·cm^{-2})	100% (10, 20 µA·cm^{-2})	[92]
V_2O_5·nH$_2$O	hydrothermal method	bilayered, 2D nanopapers/10.6	2 M Mg(CF$_3$SO$_3$)$_2$/H$_2$O	162.8 (0.2) 128 (0.3) 116.7 (0.5) 104.4 (1.0) 100.4 (2.0) 91.9 (4.0) 86 (6.0) 81.3 (10.0)	70.1% (70, 0.2) 88% (1000, 10.0)	[93]

Table 2. *Cont.*

Cathode Material	Synthesis Method	Morphology/ Interlayer Spacing, Å	Electrolyte	Specific Capacity, mAh·g^{-1} (Current Density, A·g^{-1})	Capacity Retention (Number of Cycles and Current, A·g^{-1})	Ref.
VOx-NT	hydrothermal	nanotubes	0.25 M Mg(AlBu$_2$Cl$_2$)$_2$/THF	75 (0.005)	-	[131]
VO$_x$-NT	microwave-assisted hydrothermal process	nanotubes	0.5 M Mg(ClO4)$_2$/AN	218 (0.06)	70.8% (20, 0.06)	[81]
VO$_x$-NT	microwave-assisted hydrothermal process	open-ended multilayered nanotubes	0.5 M Mg(ClO$_4$)$_2$/TMS-EA	124.0 (0.06)	50% (80, 0.06)	[82]
V$_2$O$_5$	hydrothermal synthesis	3 μm micro-spheres/25 nm thick nanosheets	0.25 M Mg(AlCl$_2$EtBu)$_2$/THF	126.2 (0.05), initial 92 (0.1) 80 (0.15) 62 (0.2)	71.9% (80, 0.05)	[76]
V$_5$O$_{12}$·6H$_2$O	hydrothermal synthesis	nanoflowers	0.8 M PhMgCl + 0.4 M AlCl$_3$/THF	234.3 (0.01) 53.2 (0.5)	82.1% (400, 0.05) 74.5% (1500, 0.1)	[78]
V$_6$O$_{13}$	Microwave-assisted	2D nanosheets/ monoclinic	1.0 M Mg(ClO$_4$)$_2$/AN	324.0 (0.02) 278.0 (0.04) 244.0 (0.06) 214.0 (0.08)	71.9% (30, 0.04)	[79]
VO$_2$ (B)	hydrothermal process	nanorods/12.093	1.0 M Mg(ClO$_4$)$_2$/AN, wet	391.0 (0.025) 370 (0.05) 341 (0.1)	94.7% (10, 0.025)	[55]
V$_2$O$_5$ nanoclusters on porous carbon frameworks	ambient hydrolysis deposition	amorphous (XRD)/ orthorhombic (^{51}V NMR)	0.2 M [Mg$_2$(μ-Cl)$_2$(DME)$_4$] [AlCl$_4$]$_2$/DME	350 (0.04), initial 225 (0.04) 180 (0.08) 120 (0.320) 100 (0.640)	75% (50, 0.04) 67% (100, 0.320)	[74]
V$_2$O$_5$/GO	Solvothermal process	microparticles, /11.512	0.25 M Mg(AlCl$_2$EtBu)$_2$/THF	178 (0.2C), initial	78.6% (20, 0.2C)	[97]
V$_2$O$_5$·1.42 H$_2$O@rGO	melt quenching process and freeze drying	nanowires /~11.3	0.5 M Mg(TFSI)$_2$/AN	320 (0.05) 280 (0.1) ~100 (2.0)	81% (200, 1.0)	[98]
V$_2$O$_5$·0.4H$_2$O/C	evaporation of solution	xerogel, bilayer	4.7 M Mg(NO$_3$)$_2$	88 (1.0), initial 102 (1.0), reversible 62 (2.0) 53 (3.0) 47 (4.0) 44 (5.0)	82.7% (10, 1.0)	[89]
V$_2$O$_3$@GO	hydrothermal/ spray-drying/annealing in Ar	3D graphene-supported nanoparticles	0.3 M Mg(TFSI)$_2$/AN	291.3 (0.05) 280.1 (0.1) 259.1 (0.2) 232.5 (0.5) 210.4 (1.0) 185.3 (2.0)	88.5% (1000, 0.5)	[99]

Table 2. *Cont.*

Cathode Material	Synthesis Method	Morphology/ Interlayer Spacing, Å	Electrolyte	Specific Capacity, mAh·g^{-1} (Current Density, A·g^{-1})	Capacity Retention (Number of Cycles and Current, A·g^{-1})	Ref.
V$_2$O$_3$@C	hydrothermal/ annealing in air/carbonization	mesoporous nanorods	0.3 M Mg(TFSI)$_2$/AN (H$_2$O)	381.0 (0.2) 354.8 (0.5) 292.7 (5.0) 208.0 (20.0) 130.4 (50.0)	60.0% (1000, 0.5)	[100]
V$_2$O$_5$-PEDOT	chemical intercala-tion/polymerization	/9.86	0.4 M APC/THF + 0.2 M CTAB	288.7 (0.1) 153.8 (0.3) 110.7 (0.5) in full cell	58% (100, 0.1) ~68% (500, 0.5)	[119]
V$_2$O$_5$/PEDOT	chemical intercala-tion/polymerization	porous, bilayered/ 19.02	0.3 M Mg(TFSI)$_2$/AN + 3M H$_2$O	339.7 (0.1), initial 256.3 (0.5), initial 320.4 (0.1), reversible 271.2 (0.2) 219.6 (0.5) 172.3 (1.0) 117.5 (2.0)	60.85% (200, 0.1) 67.3% (500, 0.5)	[120]
V$_6$O$_{13}$.PANI	solvothermal, *in situ* intercalation	nanobelts /13.4	0.5 M Mg(TFSI)$_2$/DME	195 (0.1), initial 168 (0.1), 147 (0.2) 127 (0.5) 99 (1.0) 65 (5.0) 46 (10.0)	89% (100, 0.1) 100% (2500, 5.0)	[118]
PANI-V$_2$O$_5$ (V$_2$O$_5$· 0.35C$_6$H$_6$N · 0.92H$_2$O)	intercalation of monomers and subsequent interlayer polymerization	2D organic-inorganic superlattices /15.3	0.3 M Mg(TFSI)$_2$/AN, 0.2 M Mg(CF$_3$SO$_3$)$_2$-MgCl$_2$-AlCl$_3$/DME (full cell)	280 (0.1), initial 275 (0.1), reversible 250 (0.2) 220 (0.5) 175 (1.0) 155 (2.0) 130 (4.0) 115 (0.1), full cell	70% (500, 4.0) 69.5% (50, 0.1) (full cell)	[117]
V$_2$O$_5$· 0.34H$_2$O·PAN	hydrothermal synthesis	/10.63	0.5 M Mg(TFSI)$_2$/AN	~180 (0.05), initial 143.2 (0.05) ~75 (0.5) 120.6 (0.1) (full cell, initial)	91% (18,000, 2.0) 41.5% (80, 0.1), full cell	[121]
PEO-V$_2$O$_5$	sol-gel synthesis	nanosheets /12.6	0.5 M Mg(ClO$_4$)$_2$/AN	125 (0.01), initial 100.3 (0.01)	77% (35, 0.01)	[116]
H$_2$V$_3$O$_8$	hydrothermal process	nanowires /0.467 nm	0.5 M Mg(ClO$_4$)$_2$/AN	304.2 (0.05)	89.5% (20, 0.05)	[128]
H$_2$V$_3$O$_8$	hydrothermal process	nanowires /0.34 nm	0.5 M Mg(ClO$_4$)$_2$/AN 60 °C	231 (0.01) 201 (0.02) 170 (0.04) 97 (0.08)	95.2% (30, 0.01)	[129]

Cathode Material	Synthesis Method	Morphology/ Interlayer Spacing, Å	Electrolyte	Specific Capacity, mAh·g^{-1} (Current Density, A·g^{-1})	Capacity Retention (Number of Cycles and Current, A·g^{-1})	Ref.
$H_2V_3O_8$	hydrothermal process	nanowires	$Mg(ClO_4)_2 \cdot$ 3.1 H_2O/AN	303 (0.05)	80% (30, 0.05) 61% (200, 0.1)	[130]
$H_2V_3O_8$	hydrothermal process	nanowires	0.25 M $Mg(ClO_4)_2$/AN	67 (0.05)	99% (30, 0.05) 109% (200, 0.1)	[130]
NaV_6O_{15}	hydrothermal process, annealed in air	rod-like, monoclinic /10.08	0.5 M $Mg(ClO_4)_2$/AN	213.4 (0.01), initial 210.1 (0.01) 137.0 (0.02) 111.7 (0.05) 80.2 (0.1) 52.3 (0.2) 27.2 (0.5)	87% (100, 0.02)	[103]
$Na_2V_6O_{16} \cdot$ 1.63 H_2O	hydrothermal process	nanowires /7.9	0.5 M $Mg(TFSI)_2$/DME	228 (0.02) 193 (0.03) 175 (0.05) 105 (0.08) 91 (0.1) 65 (0.2)	71% (450, 0.2)	[104]
NaV_3O_8	hydrothermal method, annealed in air	nanowires /6.85	0.5 M $Mg(ClO_4)_2$/AN	260.0 (0.05) 184.0 (0.1) 123.9 (0.2) 86.6 (0.5) 62.4 (1.0)	85.8% (30, 0.1) 88.3% (100, 0.5)	[101]
$NaV_3O_8 \cdot$ 1.69H_2O	solvothermal at RT	nanobelts	0.4 M $(PhMgCl)_2$- $AlCl_3$/THF	150.0 (0.01), initial 110.0 (0.01), 5 cycles 55.0 (0.02)	80% (100, 0.08)	[102]
$NH_4V_4O_{10}$	hydrothermal method	nanosheets/11.57	0.5 M $Mg(ClO_4)_2$/AN	175 (0.2 C) 128 (0.5 C) 110 (1.0 C) 69 (2.0 C)	36.5% (100, 1C)	[106].
Zr-$NH_4V_4O_{10}$	hydrothermal method	nanorods/11.572	0.5 M $Mg(ClO_4)_2$/AN	328 (0.04) initial 300 (0.04) 240 (0.1) 207 (0.2) 175 (0.4) 147 (0.8) 100 (0.01), full cell	86% (150, 0.04)	[105]
$Mg_{0.3}V_2O_5 \cdot$ 1.1H_2O	solvothermal	nanowires (150 nm)/11.9	0.3 M $Mg(TFSI)_2$/AN	162 (0.1) 145 (0.2) 134 (0.5) 120 (1.0) 85 (2.0) 50 (4.0)	~100% (10,000, 1.0) 80% (10,000, 2.0)	[110]

Table 2. *Cont.*

Cathode Material	Synthesis Method	Morphology/ Interlayer Spacing, Å	Electrolyte	Specific Capacity, mAh·g^{-1} (Current Density, A·g^{-1})	Capacity Retention (Number of Cycles and Current, A·g^{-1})	Ref.
Mg$_{0.1}$V$_2$O$_5$· 1.8H$_2$O	sol-gel method	agglomerates of sub-micron sized particles/ 12.3	0.5 M Mg(TFSI)$_2$/AN	300 (C/10), initial 250–280 (C/10)	93% (7, C/10)	[109]
Mg$_x$V$_5$O$_{12}$· nH$_2$O	solvothermal at near ambient conditions	nanofibers/ 11.9	0.3 M Mg(TFSI)$_2$/AN	~160 (0.05)	89% (300, 0.05) 81% (10,000, 2.0)	[108]
Mg$_{0.75}$V$_{10}$O$_{24}$· nH$_2$O	one-step precipitation method	nanoflowers/13.9	2 M Mg(CF$_3$SO$_3$)2/H$_2$O	350 (0.05) 149 (1.0) 70 (4.0)	64% (100, 3.0)	[107]
Mn$_{0.04}$V$_2$O$_5$· 1.17H$_2$O	hydrothermal method	nanobelts/ 10.9	0.3 M Mg(TFSI)$_2$/AN	145 (0.05) 131 (0.1) 110 (0.2) 108 (0.5) 97 (1.0) 80 (2.0) 50 (4.0)	82% (10,000, 2.0)	[111]
H$_{11}$Al$_2$V$_6$O$_{23.2}$	Hydrothermal method	Urchin-like microspheres/ 13.3	0.3 M Mg(TFSI)$_2$/AN	165 (0.1) 127 (0.2) 98 (0.5) 75 (1.0) 60 (2.0) 47 (4.0)	98% (50, 0.1) 87% (3000, 1.0)	[113]

4. Conclusions

RMBs are probably one of the most promising next-generation energy storage technologies due to their high theoretical energy density, high safety, abundant resources, and low cost. The design of novel cathode materials for RMBs is the focus of investigations for the future development of RMBs.

Vanadium oxide-based cathode materials present many advantages, including low cost, high safety, and great opportunity to tune the ion transport channels, which resulted in their improved electrochemical performance in RMBs.

Although great progress has been made in the development of vanadium oxide-based cathodes for RMBs, a number of challenges remain to be overcome in the future. The main challenge in the development of cathodes for RMBs is the sluggish kinetics of Mg^{2+}-ion intercalation and diffusion in electrode materials due to the strong interaction between doubly charged Mg^{2+}-ions and vanadium oxide host materials.

For the development of new cathodes with improved electrochemical performance, different synthetic procedures that allow new morphological modifications of vanadium oxide-based materials, pre-intercalation of metal ions and organic (mono- and polymeric) molecules into the interlayer space can be proposed. Pre-intercalated species act as pillars between the layers, stabilize the crystal structure of the material, and prevent amorphization and dissolution of oxides during repeated insertion/extraction of Mg^{2+}-ions. A pre-intercalation strategy allows the acquisition of materials with increased reversibility of Mg^{2+} (de)intercalation processes and increased interlayer/channel distances, which significantly improve the Mg^{2+}-ion diffusion kinetics and possibly reduce the desolvation barriers. Deeper understanding of the effects of different pre-intercalation strategies, their optimization, and their combination with other approaches will facilitate the achievement

of high-performance RMB cathodes. Further searching for possible modifiers that act as pillars represents a perspective means of cathode improvement.

Modification of vanadium oxides with highly conductive materials, such as nanocarbons, and especially conducting polymers, is also a promising means of enhancing the intrinsic conductivity of vanadium-based electrode materials and facilitating Mg^{2+} migration.

Excessive removal of interlayer water results in the loss of capacity of highly crystalline vanadium oxide structures. Mild annealing of vanadium oxides during synthesis should be considered to preserve an adequate amount of crystal water necessary to lubricate the interlayer space and weaken an interaction between oxygen sub-lattices and Mg^{2+} ions, providing electrostatic shielding. In combination with pre-intercalated metal ions or organic molecules, interlayer water also plays an important role in maintaining sufficient interlayer space. The role that traces of water in the organic electrolytes play in facilitating Mg^{2+} ion insertion also needs to be elucidated for further design of high-performance RMBs.

In addition to designing cathode materials with improved electrochemical performance, electrode/electrolyte interphase control is an important issue for stable electrochemical performance in RMBs. More attention should also be paid to the development of electrolytes compatible with cathodes and anodes.

Abbreviations

AN	acetonitrile
APC	all-phenyl complex electrolyte/phenylmagnesium chloride (PhMgCl + AlCl$_3$)
CTAB	cetyltrimethylammonium bromide
DME	dimethoxyethane
EA	ethyl acetate
G2	diglyme
PC	propylenecarbonate
PEDOT	poly(3,4-ethylenedioxythiophene)
PY$_{14}$TFSI	1-butyl-1-methylpyrrolidinium bis(trifluoromethylsulfonyl)imide
TFSI	trifluoromethylsulfonylimide
THF	tetrahydrofurane
TMS	tetramethylsilane

References

1. Yoshimoto, N.; Yakushiji, S.; Ishikawa, M.; Morita, M. Rechargeable magnesium batteries with polymeric gel electrolytes containing magnesium salts. *Electrochim. Acta* **2003**, *48*, 2317. [CrossRef]
2. Armand, M.; Tarascon, J.M. Building better batteries. *Nature* **2008**, *451*, 652. [CrossRef]
3. Levi, E.; Gofer, Y.; Aurbach, D. On the way to rechargeable Mg batteries: The challenge of new cathode materials. *Chem. Mater.* **2010**, *22*, 860. [CrossRef]
4. Yoo, H.D.; Shterenberg, I.; Gofer, Y.; Gershinsky, G.; Pour, N.; Aurbach, D. Mg rechargeable batteries: An on-going challenge. *Energ. Environ. Sci.* **2013**, *6*, 2265. [CrossRef]
5. Medina, A.; Pérez-Vicente, C.; Alcántara, R. Advancing towards a practical magnesium ion battery. *Materials* **2021**, *14*, 7488. [CrossRef] [PubMed]
6. Ma, X.F.; Li, H.Y.; Ren, W.; Gao, D.; Chen, F.; Diao, J.; Xie, B.; Huang, G.; Wang, J.; Pan, F. A critical review of vanadium-based electrode materials for rechargeable magnesium batteries. *J. Mater. Sci. Technol.* **2023**, *153*, 56–74. [CrossRef]

7.   Kulova, T.L.; Fateev, V.N.; Seregina, E.A.; Grigoriev, A.S. A brief review of post-lithium-ion batteries. *Int. J. Electrochem. Sci.* **2020**, *15*, 7242–7259. [CrossRef]

8.   Holze, R. Between the Electrodes of a Supercapacitor: An Update on Electrolytes. *Adv. Mater. Sci. Technol.* **2024**, *6*, 0627771. [CrossRef]

9.   Leong, K.W.; Pan, W.; Yi, X.; Luo, S.; Zhao, X.; Zhang, Y.; Wang, Y.; Mao, J.; Chen, Y. Next-generation magnesium-ion batteries: The quasi-solid-state approach to multivalent metal ion storage. *Sci. Adv.* **2023**, *9*, eadh1181. [CrossRef]

10. Blázquez, J.A.; Maca, R.R.; Leonet, O.; Azaceta, E.; Mukherjee, A.; Zhao-Karger, Z.; Li, Z.Y.; Kovalevsky, A.; Fernandez-Barquin, A.; Mainar, A.R.; et al. A practical perspective on the potential of rechargeable Mg batteries. *Energy Environ. Sci.* **2023**, *16*, 1964–1981. [CrossRef]

11. Wu, Y.; Holze, R. *Electrochemical Energy Conversion and Storage*; WILEY-VCH: Weinheim, Germany, 2022.

12. Huggins, R.A. *Advanced Batteries—Materials Science Aspects*; Springer: New York, NY, USA, 2009.

13. Huggins, R.A. *Energy Storage*; Springer: New York, NY, USA, 2010.

14. Shterenberg, I.; Salama, M.; Gofer, Y.; Levi, E.; Aurbach, D. The challenge of developing rechargeable magnesium batteries. *MRS Bull.* **2014**, *39*, 453–460. [CrossRef]

15. Saha, P.; Datta, M.K.; Velikokhatnyi, O.I.; Manivannan, A.; Alman, D.; Kumta, P.N. Rechargeable magnesium battery: Current status and key challenges for the future. *Prog. Mater. Sci.* **2014**, *66*, 1–86. [CrossRef]

16. Mohtadi, R.; Mizuno, F. Magnesium batteries: Current state of the art, issues and future perspectives. *Beilstein J. Nanotechnol.* **2014**, *5*, 1291–1311. [CrossRef]

17. Massé, R.C.; Uchaker, E.; Cao, G. Beyond Li-ion: Electrode materials for sodium- and magnesium-ion batteries. *Sci. China Mater.* **2015**, *58*, 715–766. [CrossRef]

18. You, C.; Wu, X.; Yuan, X.; Chen, Y.; Liu, L.; Zhu, Y.; Fu, L.; Wu, Y.; Guo, Y.G.; van Ree, T. Advances in rechargeable Mg batteries. *J. Mater. Chem. A* **2020**, *8*, 25601–25625. [CrossRef]

19. Wang, G.; Wang, Z.; Shi, H.; Du, A.; Sun, M.; Cui, G. Progress and perspective on rechargeable magnesium-ion batteries. *Sci. China Chem.* **2024**, *67*, 214–246. [CrossRef]

20. Shah, R.; Mittal, V.; Matsil, E.; Rosenkranz, A. Magnesium-ion batteries for electric vehicles: Current trends and future perspectives. *Adv. Mechan. Eng.* **2021**, *13*, 16878140211003398. [CrossRef]

21. Guo, Z.; Zhao, S.; Li, T.; Su, D.; Guo, S.; Wang, G. Recent advances in rechargeable magnesium-based batteries for high-efficiency energy storage. *Adv. Energy Mater.* **2020**, *10*, 1903591. [CrossRef]

22. Liu, F.; Wang, T.; Liu, X.; Fan, L.Z. Challenges and recent progress on key materials for rechargeable magnesium batteries. *Adv. Energy Mater.* **2021**, *11*, 2000787. [CrossRef]

23. Das, A.; Balakrishnan, N.T.M.; Sreeram, P.; Fatima, M.J.J.; Joyner, J.D.; Thakur, V.K.; Pullanchiyodan, A.; Ahn, J.H.; Raghavan, P. Prospects for magnesium ion batteries: A comprehensive materials review. *Coord. Chem. Rev.* **2024**, *502*, 215593. [CrossRef]

24. Chen, S.; Fan, S.; Li, H.; Shi, Y.; Yang, H.Y. Recent advances in kinetic optimizations of cathode materials for rechargeable magnesium batteries. *Coord. Chem. Rev.* **2022**, *466*, 214597. [CrossRef]

25. Kwon, B.J.; Lapidus, S.H.; Vaughey, J.T.; Ceder, G.; Cabana, J.; Key, B. Design strategies of spinel oxide frameworks enabling reversible mg-ion intercalation. *Acc. Chem. Res.* **2024**, *57*, 1–9. [CrossRef] [PubMed]

26. Zhang, J.; Wang, X.; Li, H.; Zhang, H.; Zhang, Y.; Wang, K. Layered materials in the magnesium ion batteries: Development history, materials structure, and energy storage mechanism. *Adv. Funct. Mater.* **2023**, *33*, 2301974. [CrossRef]

27. Huie, M.M.; Bock, D.; Takeuchi, E.S.; Marschilok, A.C.; Takeuchi, K.J. Cathode materials for magnesium and magnesium-ion based batteries. *Coord. Chem. Rev.* **2015**, *287*, 15–27. [CrossRef]

28. Canepa, P.; Sai Gautam, G.; Hannah, D.C.; Malik, R.; Liu, M.; Gallagher, K.G.; Persson, K.A.; Ceder, G. Odyssey of multivalent cathode materials: Open questions and future challenges. *Chem. Rev.* **2017**, *117*, 4287–4341. [CrossRef] [PubMed]

29. Mao, M.; Gao, T.; Hou, S.; Wang, C. A critical review of cathodes for rechargeable Mg batteries. *Chem. Soc. Rev.* **2018**, *47*, 8804–8841. [CrossRef] [PubMed]

30. Ma, Z.; MacFarlane, D.R.; Kar, M. Mg cathode materials and electrolytes for rechargeable Mg batteries: A review. *Batter. Supercaps* **2019**, *2*, 115–127. [CrossRef]

31. Liu, Y.; He, G.; Jiang, H.; Parkin, I.P.; Shearing, P.R.; Brett, D.J.L. Cathode design for aqueous rechargeable multivalent ion batteries: Challenges and opportunities. *Adv. Funct. Mater.* **2021**, *31*, 2010445. [CrossRef]

32. Pryke, J.J.; Kennard, R.M.; Cussen, S.A. Cathodes for Mg batteries: A condensed review. *Energy Rep.* **2022**, *8*, 83–88. [CrossRef]

33. Li, Z.; Häcker, J.; Fichtner, M.; Zhao-Karger, Z. Cathode materials and chemistries for magnesium batteries: Challenges and opportunities. *Adv. Energy Mater.* **2023**, *13*, 2300682. [CrossRef]

34. Zhang, M.; Feng, S.; Wu, Y.; Li, Y. Cathode Materials for Rechargeable Magnesium-Ion Batteries: A Review. *Acta Phys. Chim. Sin.* **2023**, *39*, 2205050. [CrossRef]

35. Kotobuki, M.; Yan, B.; Lu, L. Recent progress on cathode materials for rechargeable magnesium batteries. *Energy Storage Mater.* **2023**, *54*, 227–253. [CrossRef]

36. Shi, M.; Li, T.; Shang, H.; Zhang, D.; Qi, H.; Huang, T.; Xie, Z.; Qi, J.; Wie, F. A critical review of inorganic cathode materials for rechargeable magnesium ion batteries. *J. Energy Storage* **2023**, *68*, 107765. [CrossRef]

37. Zhang, J.; Chang, Z.; Zhang, Z.; Du, A.; Dong, S.; Li, Z.; Li, G.; Cui, G. Current design strategies for rechargeable magnesium-based batteries. *ACS Nano* **2021**, *15*, 15594. [CrossRef] [PubMed]

38. Li, L.; Lu, Y.; Zhang, Q.; Zhao, S.; Hu, Z.; Chou, S.L. Recent progress on layered cathode materials for nonaqueous rechargeable magnesium batteries. *Small* **2021**, *17*, 201902767. [CrossRef]

39. Xu, R.; Gao, X.; Chen, Y.; Chen, X.; Cui, L. Research status and prospect of rechargeable magnesium ion batteries cathode materials. *Chin. Chem. Lett.* **2024**, *35*, 109852. [CrossRef]

40. Maroni, F.; Dongmo, S.; Gauckler, C.; Marinaro, M.; Wohlfahrt-Mehrens, M. Through the maze of multivalent-ion batteries: A critical review on the status of the research on cathode materials for Mg^{2+} and Ca^{2+} ions insertion. *Batter. Supercaps* **2021**, *4*, 1221–1251. [CrossRef]

41. Attias, R.; Sharon, D.; Goffer, Y.; Aurbach, D. Critical review on the unique interactions and electroanalytical challenges related to cathodes—*Solutions* interfaces in non-aqueous Mg battery prototypes. *ChemElectroChem* **2021**, *8*, 3229. [CrossRef]

42. Li, M.; Ding, Y.; Sun, Y.; Ren, Y.; Yang, J.; Yin, B.; Li, H.; Zhang, S.; Ma, T. Emerging rechargeable aqueous magnesium ion battery. *Mater. Rep. Energy* **2022**, *2*, 100161. [CrossRef]

43. Javed, M.; Shah, A.; Nisar, J.; Shahzad, S.; Haleem, A.; Shah, I. Nanostructured design cathode materials for magnesium-ion batteries. *ACS Omega* **2024**, *9*, 4229–4245. [CrossRef]

44. Mensing, J.P.; Lomas, T.; Tuantranont, A. Advances in rechargeable magnesium batteries employing graphene-based materials. *Carbon* **2022**, *197*, 264–281. [CrossRef]

45. Zhang, X.; Li, D.; Ruan, Q.; Liu, L.; Wang, B.; Xiong, F.; Huang, C.; Chu, P.K. Vanadium-based cathode materials for rechargeable magnesium batteries. *Mater. Today Energy* **2023**, *32*, 101232. [CrossRef]

46. Guo, W.; Fu, D.; Song, H.; Wang, C. Advanced V-based materials for multivalent-ion storage applications. *Energy Mater* **2024**, *4*, 400026. [CrossRef]

47. Johnston, B.; Henry, H.; Kim, N.; Lee, S.B. Mechanisms of water-stimulated Mg^{2+} intercalation in vanadium oxide: Toward the development of hydrated vanadium oxide cathodes for Mg batteries. *Front. Energy Res.* **2021**, *8*, 611391. [CrossRef]

48. Esparcia, E., Jr.; Joo, J.; Lee, J. Vanadium oxide bronzes as cathode active materials for non-lithium-based batteries. *CrystEngComm* **2021**, *23*, 5267–5283. [CrossRef]

49. Alcantara, R.; Lavela, P.; Edstrom, K.; Fichtner, M.; Le, T.K.; Floraki, C.; Aivaliotis, D.; Vernardou, D. Metal-ion intercalation mechanisms in vanadium pentoxide and its new perspectives. *Nanomaterials* **2023**, *13*, 3149. [CrossRef] [PubMed]

50. Park, S.K.; Dose, W.M.; Boruah, B.D.; De Volder, M. In situ and operando analyses of reaction mechanisms in vanadium oxides for Li-, Na-, Zn-, and Mg-ions batteries. *Adv. Mater. Technol.* **2022**, *7*, 2100799. [CrossRef]

51. Hu, P.; Hu, P.; Vu, T.D.; Li, M.; Wang, S.; Ke, Y.; Zeng, X.; Mai, L.; Long, Y. Vanadium oxide: Phase diagrams, structures, synthesis, and applications. *Chem. Rev.* **2023**, *123*, 4353–4415. [CrossRef] [PubMed]

52. Cestarolli, D.T.; Guerra, E.M. Vanadium pentoxide (V_2O_5): Their obtaining methods and wide applications. In *Transition Metal Compounds—Synthesis, Properties and Applications*; Haider, S., Haider, A., Eds.; IntechOpen: London, UK, 2021; pp. 1–15.

53. Kuang, C.; Zeng, W.; Li, Y. A review of electrode for rechargeable magnesium-ion batteries. *J. Nanosci. Nanotechnol.* **2019**, *19*, 12–25. [CrossRef]

54. Zhao, X.; Mao, L.; Cheng, Q.; Liao, F.; Yang, G.; Lu, X. Interlayer engineering of preintercalated layered oxides as cathode for emerging multivalent metal-ion batteries: Zinc and beyond. *Energy Storage Mater.* **2021**, *38*, 397–437. [CrossRef]

55. Luo, T.; Liu, Y.; Su, H.; Xiao, R.; Huang, L.; Xiang, Q.; Zhou, Y.; Chen, C. Nanostructured-VO_2(B): A high-capacity magnesium-ion cathode and its electrochemical reaction mechanism. *Electrochim. Acta* **2018**, *260*, 805–813. [CrossRef]

56. Setiawan, D.; Chae, M.S.; Hong, S.T. Re-evaluating the magnesium-ion storage capability of vanadium dioxide, VO_2(B): Uncovering the influence of water content on the previously overestimated high capacity. *ChemSusChem* **2023**, *16*, e202300758. [CrossRef] [PubMed]

57. He, Y.; Xu, H.; Bian, H.; Ge, Q.; Li, D.; Wang, A.; Sun, D. Synergistic effect of V_3O_7/VO_2 film electrodes as high-performance cathode materials for magnesium-ion batteries. *Solid State Sci.* **2024**, *149*, 107445. [CrossRef]

58. Livage, J. Vanadium pentoxide gels. *Chem. Mater.* **1991**, *3*, 578–593. [CrossRef]

59. Yu, W.H.; Wang, D.Z.; Zhu, B.; Wang, S.J.; Xue, L.X. Insertion of bi-valence cations Mg^{2+} and Zn^{2+} into V_2O_5. *Solid State Commun.* **1987**, *61*, 271–273. [CrossRef]

60. Gregory, T.D.; Hoffman, R.J.; Winterton, R.C. Nonaqueous electrochemistry of magnesium: Applications to energy storage. *J. Electrochem. Soc.* **1990**, *137*, 775–780. [CrossRef]

61. Novák, P.; Desilvestro, J. Electrochemical insertion of magnesium in metal oxides and sulfides from aprotic electrolytes. *J. Electrochem. Soc.* **1993**, *140*, 140–144. [CrossRef]

62. Amatucci, G.G.; Badway, F.; Singhal, A.; Beaudoin, B.; Skandan, G.; Bowmer, T.; Plitz, I.; Pereira, N.; Chapman, T.; Jaworski, R. Investigation of yttrium and polyvalent ion intercalation into nanocrystalline vanadium oxide. *J. Electrochem. Soc.* **2001**, *148*, A940–A950. [CrossRef]

63. Gautam, G.S.; Canepa, P.; Abdellahi, A.; Urban, A.; Malik, R.; Ceder, G. The intercalation phase diagram of Mg in V_2O_5 from first-principles. *Chem. Mater.* **2015**, *27*, 3733–3742.

64. Gautam, G.S.; Canepa, P.; Malik, R.; Liu, M.; Persson, K.; Ceder, G. First-principles evaluation of multi-valent cation insertion into orthorhombic V_2O_5. *Chem. Commun.* **2015**, *51*, 13619–13622. [CrossRef]

65. Xiao, R.; Xie, J.; Luo, T.; Huang, L.; Zhou, Y.; Yu, D.; Chen, C.; Liu, Y. Phase transformation and diffusion kinetics of V_2O_5 electrode in rechargeable Li and Mg batteries: A first-principle study. *J. Phys. Chem. C* **2018**, *122*, 1513–1521. [CrossRef]

66. Kulish, V.V.; Manzhos, S. Comparison of Li, Na, Mg and Al-ion insertion in vanadium pentoxides and vanadium dioxides. *RSC Adv.* **2017**, *7*, 18643–18649. [CrossRef]

67. Trócoli, R.; Parajuli, P.; Frontera, C.; Black, A.P.; Alexander, G.C.B.; Roy, I.; Arroyo-de Dompablo, M.E.; Klie, R.F.; Cabana, J.; Palacín, M.R. β-V_2O_5 as magnesium intercalation cathode. *ACS Appl. Energy Mater.* **2022**, *5*, 11964–11969. [CrossRef]

68. Parija, A.; Liang, Y.; Andrews, J.L.; De Jesus, L.R.; Prendergast, D.; Banerjee, S. Topochemically de-intercalated phases of V_2O_5 as cathode materials for multivalent intercalation batteries: A first-principles evaluation. *Chem. Mater.* **2016**, *28*, 5611–5620. [CrossRef]

69. Andrews, J.L.; Mukherjee, A.; Yoo, H.D.; Parija, A.; Marley, P.M.; Fakra, S.; Prendergast, D.; Cabana, J.; Klie, R.F.; Banerjee, S. Reversible Mg-ion insertion in a metastable one-dimensional polymorph of V_2O_5. *Chem* **2018**, *4*, 564–585. [CrossRef]

70. Johnson, I.D.; Nolis, G.; Yin, L.; Yoo, H.D.; Parajuli, P.; Mukherjee, A.; Andrews, J.L.; Lopez, M.; Klie, R.F.; Banerjee, S.; et al. Enhanced charge storage of nanometric ζ-V_2O_5 in Mg electrolytes. *Nanoscale* **2020**, *12*, 22150–22160. [CrossRef]

71. Gershinsky, G.; Yoo, H.D.; Gofer, Y.; Aurbach, D. Electrochemical and spectroscopic analysis of Mg^{2+} intercalation into thin film electrodes of layered oxides: V_2O_5 and MoO_3. *Langmuir* **2013**, *29*, 10964–10972. [CrossRef]

72. Yoo, H.D.; Jokisaari, J.R.; Yu, Y.S.; Kwon, B.J.; Hu, L.; Kim, S.; Han, S.D.; Lopez, M.; Lapidus, S.H.; Nolis, G.M.; et al. Intercalation of magnesium into a layered vanadium oxide with high capacity. *ACS Energy Lett.* **2019**, *4*, 1528–1534. [CrossRef]

73. Drosos, C.; Jia, C.; Mathew, S.; Palgrave, R.G.; Moss, B.; Kafizas, A.; Vernardou, D. Aerosol-assisted chemical vapor deposition of V_2O_5 cathodes with high rate capabilities for magnesium-ion batteries. *J. Power Sources* **2018**, *384*, 355–359. [CrossRef]

74. Cheng, Y.; Shao, Y.; Raju, V.; Ji, X.; Mehdi, B.L.; Han, K.S.; Engelhard, M.H.; Li, G.; Browning, N.D.; Mueller, K.T.; et al. Molecular storage of Mg ions with vanadium oxide nanoclusters. *Adv. Funct. Mater.* **2016**, *26*, 3446–3453. [CrossRef]

75. Fu, Q.; Sarapulova, A.; Trouillet, V.; Zhu, L.; Fauth, F.; Mangold, S.; Welter, E.; Indris, S.; Knapp, M.; Dsoke, S.; et al. In operando synchrotron diffraction and in operando X-ray absorption spectroscopy investigations of orthorhombic V_2O_5 nanowires as cathode materials for Mg-ion batteries. *J. Am. Chem. Soc.* **2019**, *141*, 2305–2315. [CrossRef] [PubMed]

76. Xiao, Y.; Pan, M.; Zou, J.; Guo, R.; Zeng, X.; Ding, W. Surfactant induced formation of flower-like V_2O_5 microspheres as cathode materials for rechargeable magnesium batteries. *Ionics* **2019**, *25*, 5889–5897. [CrossRef]

77. Mukherjee, A.; Taragin, S.; Aviv, H.; Perelshtein, I.; Noked, M. Rationally designed vanadium pentoxide as high capacity insertion material for Mg-ion. *Adv. Funct. Mater.* **2020**, *30*, 2003518. [CrossRef]

78. Man, Y.; Fei, Y.; Duan, L.; Tian, R.; Li, A.; Yuan, Z.; Zhou, X. Self-assembled vanadium oxide nanoflowers as a high-efficiency cathode material for magnesium-ion batteries. *Chem. Eng. J.* **2023**, *472*, 145118. [CrossRef]

79. Wang, Z.; Zhang, Y.; Xiao, S.; Zhai, H.; Zhu, Y.; Cao, C. Microwave-assisted synthesis of metallic V_6O_{13} nanosheet as high-capacity cathode for magnesium storage. *Mater. Lett.* **2022**, *308*, 131279. [CrossRef]

80. Jiao, L.; Yuan, H.; Wang, Y.; Cao, J.; Wang, Y. Mg intercalation properties into open-ended vanadium oxide nanotubes. *Electrochem. Commun.* **2005**, *7*, 431–436. [CrossRef]

81. Kim, R.H.; Kim, J.S.; Kim, H.J.; Chang, W.S.; Han, D.W.; Lee, S.S.; Doo, S.G. Highly reduced VOx nanotube cathode materials with ultra-high capacity for magnesium ion batteries. *J. Mater. Chem. A* **2014**, *2*, 20636. [CrossRef]

82. Kim, J.S.; Kim, R.H.; Yun, D.J.; Lee, S.S.; Doo, S.G.; Kim, D.Y.; Kim, H. Cycling stability of a VOx nanotube cathode in mixture of ethyl acetate and tetramethylsilane-based electrolytes for rechargeable Mg-ion batteries. *ACS Appl. Mater. Interfaces* **2016**, *8*, 26657–26663. [CrossRef] [PubMed]

83. Christensen, C.K.; Bojesen, E.D.; Sørensen, D.R.; Kristensen, J.H.; Mathiesen, J.K.; Iversen, B.B.; Ravnsbæk, D.B. Structural evolution during Li- and Mg-intercalation in vanadium oxide nanotube electrodes for battery applications. *ACS Appl. Nano Mater.* **2018**, *1*, 5071–5082. [CrossRef]

84. Tang, P.E.; Sakamoto, J.S.; Baudrin, E.; Dunn, B. V_2O_5 aerogel as a versatile host for metal ions. *J. Non-Cryst. Solids* **2004**, *350*, 67–72. [CrossRef]

85. Le, D.B.; Passerini, S.; Coustier, F.; Guo, J.; Soderstrom, T.; Owens, B.B.; Smyrl, W.H. Intercalation of polyvalent cations into V_2O_5 aerogels. *Chem. Mater.* **1998**, *10*, 682–684. [CrossRef]

86. Moretti, A.; Passerini, S. Bilayered nanostructured $V_2O_5 \cdot nH_2O$ for metal batteries. *Adv. Energy Mater.* **2016**, *6*, 1600868. [CrossRef]

87. Stojković, I.; Cvjetićanin, N.; Markovic, S.; Mitrić, M.; Mentus, S. Electrochemical behavior of V_2O_5 xerogel and V_2O_5 xerogel/C composite in an aqueous $LiNO_3$ and $Mg(NO_3)_2$ solutions. *Acta Phys. Pol. A* **2010**, *117*, 837–840. [CrossRef]

88. Inamoto, M.; Kurihara, H.; Yajima, T. Electrode performance of vanadium pentoxide xerogel prepared by microwave irradiation as an active cathode material for rechargeable magnesium batteries. *Electrochemistry* **2012**, *80*, 421–422. [CrossRef]

89. Vujković, M.; Pašti, I.; Simatović, I.; Šljukić, B.; Milenković, M.; Mentus, S. The influence of intercalated ions on cyclic stability of V_2O_5/graphite composite in aqueous electrolytic solutions: Experimental and theoretical approach. *Electrochim. Acta* **2015**, *176*, 130–140. [CrossRef]

90. Sai Gautam, G.; Canepa, P.; Richards, W.D.; Malik, R.; Ceder, G. Role of structural H_2O in intercalation electrodes: The case of Mg in nanocrystalline xerogel-V_2O_5. *Nano Lett.* **2016**, *16*, 2426–2431. [CrossRef] [PubMed]

91. Tepavcevic, S.; Liu, Y.; Zhou, D.; Uti, B.; Maser, J.; Zuo, X.; Chan, H.; Král, P.; Johnson, C.S.; Stamenkovic, V.; et al. Nanostructured layered cathode for rechargeable Mg-ion batteries. *ACS Nano* **2015**, *9*, 8194–8205. [CrossRef] [PubMed]

92. Sa, N.Y.; Kinnibrugh, T.L.; Wang, H.; Gautam, G.S.; Chapman, G.W.; Vaughey, J.T.; Key, B.; Fister, T.T.; Freeland, J.W.; Proffit, D.L.; et al. Structural evolution of reversible Mg insertion into a bilayer structure of $V_2O_5 \cdot nH_2O$ xerogel material. *Chem. Mater.* **2016**, *28*, 2962–2969. [CrossRef]

93. He, Q.; Wang, H.; Bai, J.; Liao, Y.; Wang, S.; Chen, L. Bilayered nanostructured V_2O_5 nH_2O xerogel constructed 2D nano-papers for efficient aqueous zinc/magnesium ion storage. *J. Colloid Interf. Sci.* **2024**, *662*, 490–504. [CrossRef]

94. Imamura, D.; Miyayama, M. Characterization of magnesium-intercalated V_2O_5/carbon composites. *Solid State Ion.* **2003**, *161*, 173–180. [CrossRef]

95. Imamura, D.; Miyayama, M.; Hibino, M.; Kudo, T. Mg intercalation properties into V_2O_5 gel/carbon composites under high-rate condition. *J. Electrochem. Soc.* **2003**, *150*, A753–A758. [CrossRef]

96. Sheha, E.; Makled, M.; Nouman, W.M.; Bassyouni, A.; Yaghmour, S.; Abo-Elhassan, S. Vanadium oxide/graphene nanoplatelet as a cathode material for Mg-ion battery. *Graphene* **2016**, *5*, 178–188. [CrossRef]

97. Du, X.; Huang, G.; Qin, Y.; Wang, L. Solvothermal synthesis of GO/V_2O_5 composites as a cathode material for rechargeable magnesium batteries. *RSC Adv.* **2015**, *5*, 76352–76355. [CrossRef]

98. An, Q.; Li, Y.; Yoo, H.D.; Chen, S.; Ru, Q.; Mai, L.; Yao, Y. Graphene decorated vanadium oxide nanowire aerogel for long cycle-life magnesium battery cathodes. *Nano Energy* **2015**, *18*, 265–272. [CrossRef]

99. Pei, C.Y.; Jin, M.D.; Yin, Y.M.; Xiong, F.Y.; Jiang, Y.L.; Yuan, X.F.; Wang, F.; An, Q.Y. Intercalation-type V_2O_3 with fast Mg^{2+} diffusion kinetics for high-capacity and long-life Mg-ion storage. *ACS Sustain. Chem. Eng.* **2020**, *8*, 16164–16171. [CrossRef]

100. Jang, G.; Joe, Y.S.; Lee, S.J.; Cho, H.G.; Baek, S.H.; Xiong, P.; Shin, K.H.; Yeon, J.S.; Kang, M.S.; Oh, S.H.; et al. Crystal reconstruction of V_2O_3/carbon heterointerfaces via anodic hydration for ultrafast and reversible Mg-ion battery cathodes. *InfoMat* **2024**, *6*, e12517. [CrossRef]

101. Tang, H.; Xiong, F.; Jiang, Y.; Pei, C.; Tan, S.; Yang, W.; Li, M.; An, Q.; Mai, L. Alkali ions pre-intercalated layered vanadium oxide nanowires for stable magnesium ions storage. *Nano Energy* **2019**, *58*, 347–354. [CrossRef]

102. Rashad, M.; Zhang, H.; Asif, M.; Feng, K.; Li, X.; Zhang, H. Low-Cost Room-Temperature Synthesis of $NaV_3O_8 \cdot 1.69H_2O$ Nanobelts for Mg Batteries. *ACS Appl. Mater. Interfaces* **2018**, *10*, 4757–4766. [CrossRef]

103. Wu, D.; Zeng, J.; Hua, H.; Wu, J.; Yang, Y.; Zhao, J. NaV_6O_{15}: A promising cathode material for insertion/extraction of Mg^{2+} with excellent cycling performance. *Nano Res.* **2020**, *13*, 335–343. [CrossRef]

104. Sun, R.; Ji, X.; Luo, C.; Hou, S.; Hu, P.; Pu, X.; Cao, L.; Mai, L.; Wang, C. Water-pillared sodium vanadium bronze nanowires for enhanced rechargeable magnesium ion storage. *Small* **2020**, *16*, 2000741. [CrossRef]

105. Muthuraj, D.; Sarkar, A.; Panda, M.R.; Adil, M.; Sagdeo, A.; Mitra, S. Zirconium-doped vanadium oxide and ammonium linked layered cathode to construct a full-cell magnesium-ion battery: A Realization and structural, electrochemical Study. *Batter. Supercaps* **2021**, *4*, 1757–1770. [CrossRef]

106. Esparcia, E.A.; Chae, M.S.; Ocon, J.D.; Hong, S.T. Ammonium vanadium bronze ($NH_4V_4O_{10}$) as a high-capacity cathode material for nonaqueous magnesium-ion batteries. *Chem. Mater.* **2018**, *30*, 3690–3696. [CrossRef]

107. Ma, X.F.; Zhao, B.Q.; Liu, H.; Tan, J.; Li, H.Y.; Zhang, X.; Diao, J.; Yue, J.; Huang, G.; Wang, J. H_2O-Mg^{2+} waltz-like shuttle enables high-capacity and ultralong-life magnesium-ion batteries. *Adv. Sci.* **2024**, *11*, 2401005. [CrossRef]

108. Zhu, Y.; Huang, G.; Yin, J.; Lei, Y.; Emwas, A.H.; Yu, X.; Mohammed, O.F.; Alshareef, H.N. Hydrated $Mg_xV_5O_{12}$ cathode with improved Mg^{2+} storage performance. *Adv. Energy Mater.* **2020**, *10*, 2002128. [CrossRef]

109. Lee, S.H.; DiLeo, R.A.; Marschilok, A.C.; Takeuchi, K.J.; Takeuchi, E.S. Sol gel based synthesis and electrochemistry of magnesium vanadium oxide: A promising cathode material for secondary magnesium ion batteries. *ECS Electrochem. Lett.* **2014**, *3*, A87–A90. [CrossRef]

110. Xu, Y.; Deng, X.; Li, Q.; Zhang, G.; Xiong, F.; Tan, S.; Wei, Q.; Lu, J.; Li, J.; An, Q. Vanadium oxide pillared by interlayer Mg^{2+} ions and water as ultralong-life cathodes for magnesium-ion batteries. *Chem* **2019**, *5*, 1194–1209. [CrossRef]

111. Deng, X.; Xu, Y.; An, Q.; Xiong, F.; Tan, S.; Wu, L.; Mai, L. Manganese ion pre-intercalated hydrated vanadium oxide as a high-performance cathode for magnesium ion batteries. *J. Mater. Chem. A* **2019**, *7*, 10644–10650. [CrossRef]

112. Fu, Q.; Wu, X.; Luo, X.; Ding, Z.; Indris, S.; Sarapulova, A.; Meng, Z.; Desmau, M.; Wang, Z.; Hua, W. Ca^{2+} pre-intercalated bilayered vanadium oxide for high-performance aqueous Mg-ion batteries. *Energy Storage Mater.* **2024**, *66*, 103212. [CrossRef]

113. Tang, H.; Chao, F.; Chen, H.; Jia, R.; Luo, H.; Xiong, F.; Yao, X.; Zhang, W.; Zuo, C.; Wang, J. Water-lubricated aluminum vanadate for enhanced rechargeable magnesium ion storage. *Small* **2022**, *18*, 2203525. [CrossRef] [PubMed]

114. Yin, J.; Pelliccione, C.J.; Lee, S.H.; Takeuchi, E.S.; Takeuchi, K.J.; Marschilok, A.C. Sol-gel synthesized magnesium vanadium oxide, $Mg_xV_2O_5 \cdot nH_2O$: The role of structural Mg^{2+} on battery performance. *J. Electrochem. Soc.* **2016**, *163*, A1941–A1943. [CrossRef]

115. Tolstopyatova, E.G.; Kamenskii, M.A.; Kondratiev, V.V. Vanadium oxide–conducting polymers composite cathodes for aqueous zinc-ion batteries: Interfacial design and enhancement of electrochemical performance. *Energies* **2022**, *15*, 8966. [CrossRef]

116. Perera, S.D.; Archer, R.B.; Damin, C.A.; Mendoza-Cruz, R.; Rhodes, C.P. Controlling interlayer interactions in vanadium pentoxide-poly(ethylene oxide) nanocomposites for enhanced magnesium-ion charge transport and storage. *J. Power Sources* **2017**, *343*, 580–591. [CrossRef]

117. Zuo, C.; Xiao, Y.; Pan, X.; Xiong, F.; Zhang, W.; Long, J.; Dong, S.; An, Q.; Luo, P. Organic-inorganic superlattices of vanadium oxide@polyaniline for high-performance magnesium-ion batteries. *ChemSusChem* **2021**, *14*, 2093–2099. [CrossRef] [PubMed]

118. Kong, H.; Ou, J.; Chen, L.; Sun, W.; Fu, F.; Zhang, H.; Chen, H. Interlayer engineering in V_6O_{13} nanobelts toward superior Mg-ion storage. *Inorg. Chem. Front.* **2022**, *10*, 544–551. [CrossRef]

119. Yao, Z.; Yu, Y.; Wu, Q.; Cui, M.; Zhou, X.; Liu, J.; Li, C. Maximizing magnesiation capacity of nanowire cluster oxides by conductive macromolecule pillaring and multication intercalation. *Small* **2021**, *17*, 2102168. [CrossRef] [PubMed]

120. Joe, Y.S.; Kang, M.S.; Jang, G.; Lee, S.J.; Nakhanivei, P.; Baek, S.H.; Kim, Y.K.; Jeong, G.; Kim, H.S.; Park, H.S. Intercalation of bilayered V_2O_5 by electronically coupled PEDOT for greatly improved kinetic performance of magnesium ion battery cathodes. *Chem. Eng. J.* **2023**, *460*, 141706. [CrossRef]

121. Deng, R.; Wang, Z.; Tan, S.; Huang, X.; Gao, Z.; Fang, Y.; Chen, C.; Wang, R.; Xu, C.; Huang, G.; et al. Optimization of the electrode reaction kinetics of V_2O_5 via polyacrylonitrile intercalation for high-performance magnesium batteries. *Chem. Eng. J.* **2024**, *489*, 151095. [CrossRef]

122. Mukherjee, A.; Sa, N.; Phillips, P.J.; Burrell, A.; Vaughey, J.; Klie, R.F. Direct investigation of Mg intercalation into the orthorhombic V_2O_5 cathode using atomic-resolution transmission electron microscopy. *Chem. Mater.* **2017**, *29*, 2218–2226. [CrossRef]

123. Verrelli, R.; Black, A.P.; Pattanathummasid, C.; Tchitchekova, D.S.; Ponrouch, A.; Oro-Sol, J.; Frontera, C.; Bard, F.; Rozier, P.; Palacín, M.R. On the strange case of divalent ions intercalation in V_2O_5. *J. Power Sources* **2018**, *407*, 162–172. [CrossRef]

124. Yu, L.; Zhang, X. Electrochemical insertion of magnesium ions into V_2O_5 from aprotic electrolytes with varied water content. *J. Colloid Interface Sci.* **2004**, *278*, 160–165. [CrossRef]

125. Sa, N.; Wang, H.; Proffit, D.L.; Lipson, A.L.; Key, B.; Liu, M.; Feng, Z.; Fister, T.T.; Ren, Y.; Sun, C.J.; et al. Is α-V_2O_5 a cathode material for Mg insertion batteries? *J. Power Sources* **2016**, *323*, 44–50. [CrossRef]

126. Lim, S.C.; Lee, J.; Kwak, H.H.; Heo, J.W.; Chae, M.S.; Ahn, D.; Jang, Y.H.; Lee, H.; Hong, S.T. Unraveling the magnesium-ion intercalation mechanism in vanadium pentoxide in a wet organic electrolyte by structural determination. *Inorg. Chem.* **2017**, *56*, 7668–7678. [CrossRef] [PubMed]

127. Novák, P.; Scheifele, W.; Joho, F.; Haas, O. Electrochemical insertion of magnesium into hydrated vanadium bronzes. *J. Electrochem. Soc.* **1995**, *142*, 2544–2550. [CrossRef]

128. Tang, H.; Xu, N.; Pei, C.; Xiong, F.; Tan, S.; Luo, W.; An, Q.; Mai, L. $H_2V_3O_8$ nanowires as high-capacity cathode materials for magnesium-based battery. *ACS Appl. Mater. Interfaces* **2017**, *9*, 28667–28673. [CrossRef] [PubMed]

129. Rastgoo-Deylami, M.; Chae, M.S.; Hong, S.T. $H_2V_3O_8$ as a high energy cathode material for nonaqueous magnesium-ion batteries. *Chem. Mater.* **2018**, *30*, 7464–7472. [CrossRef]

130. Söllinger, D.; Redhammer, G.J.; Schoiber, J.; Zickler, G.A.; Pokrant, S. Exploring the insertion properties of Mg^{2+} in $H_2V_3O_8$ as a function of the water content in the organic electrolyte. *Electrochim. Acta* **2022**, *434*, 141294. [CrossRef]

131. Jiao, L.; Yuan, H.; Si, Y.; Wang, Y.; Cao, J.; Gao, X.; Zhao, M.; Zhou, X.; Wang, Y. Electrochemical insertion of magnesium in open-ended vanadium oxide nanotubes. *J. Power Sources* **2006**, *156*, 673–676. [CrossRef]